

# Multi-wavelength landscape of the young galaxy cluster RXJ 1257.2+4738 at $z = 0.866$

## II. Morphological properties<sup>★</sup>

I. Pintos-Castro<sup>1,2,3,4</sup>, M. Pović<sup>5</sup>, M. Sánchez-Portal<sup>6,4</sup>, J. Cepa<sup>3,2</sup>, B. Altieri<sup>6</sup>, Á. Bongiovanni<sup>2,3</sup>, P. A. Duc<sup>7</sup>,  
A. Ederoclite<sup>8</sup>, I. Oteo<sup>9,10</sup>, A. M. Pérez García<sup>2,3</sup>, R. Pérez Martínez<sup>6,4</sup>, J. Polednikova<sup>2,3</sup>,  
M. Ramón-Pérez<sup>2,3</sup>, and S. Tempurin<sup>11</sup>

<sup>1</sup> Centro de Astrobiología, INTA-CSIC, 28691 Villanueva de la Cañada, Madrid, Spain  
e-mail: ipintos@cab.inta-csic.es

<sup>2</sup> Instituto de Astrofísica de Canarias, 38205 La Laguna, Tenerife, Spain

<sup>3</sup> Departamento de Astrofísica, Facultad de Física, Universidad de La Laguna, 38205 La Laguna, Tenerife, Spain

<sup>4</sup> ISDEFE, Madrid, Spain

<sup>5</sup> Instituto de Astrofísica de Andalucía (IAA-CSIC), 18071 Granada, Spain

<sup>6</sup> European Space Astronomy Centre (ESAC), 38205 Villanueva de la Cañada, Madrid, Spain

<sup>7</sup> Laboratoire AIM Saclay, CEA/IRFU, CNRS/INSU, Université Paris Diderot, 75000 Paris, France

<sup>8</sup> Centro de Estudios de Física del Cosmos de Aragón, 44001 Teruel, Spain

<sup>9</sup> Institute for Astronomy, University of Edinburgh, Royal Observatory, Edinburgh, UK

<sup>10</sup> European Southern Observatory, Garching, Germany

<sup>11</sup> Institute of Astro- and Particle Physics, University of Innsbruck, Austria

Received 15 June 2015 / Accepted 3 May 2016

### ABSTRACT

Studying the evolution of the morphological distribution of galaxies in different environments can provide important information about the effects of the environment and the physical mechanisms responsible for the morphological transformations. As part of a complete analysis of the young cluster RXJ 1257+4738 at  $z \sim 0.9$ , in this work we study the morphological properties of its galaxies. We used non-parametric methods of morphological classification, as implemented in the galSVM code. The classification with the applied method was possible even using ground-based observations, as the  $r'$ -band imaging from OSIRIS/GTC. We defined very conservative probability limits, taking into account the probability errors, to obtain a trustworthy classification. In this way we were able to classify  $\sim 30\%$  of all cluster members and to separate between late-type (LT) and early-type (ET) galaxies. Additionally, when analysing the colour-magnitude diagram, we observed a significant population of blue ET galaxies among the classified ones. We discussed possible explanations for finding this population. Moreover, we studied different physical properties of LT, ET, and blue ET galaxies. They turn out to be comparable, with the exception of the stellar mass that shows that the red ET population is more massive. We also analysed the morphology-density and morphology-radius relations observing that, only when considering the morphological separation between ET and LT galaxies, a mild classical behaviour is obtained. RXJ 1257+4738 is a young galaxy cluster, showing a clumpy structure, which is still in the process of formation, and which could explain the lack of some of the standard morphological relations. This makes this cluster a very attractive case for obtaining higher resolution data and for studying the morphological properties of the entire cluster in more detail and their relation to the environment.

**Key words.** galaxies: clusters: individual: RXJ 1257.2+4738 – galaxies: evolution

## 1. Introduction

The cores of nearby clusters are dominated by red, massive, and passive elliptical and S0 galaxies, whereas there are significant changes in galaxy properties towards the outer parts of clusters, notably the increase in the percentage of late-type galaxies. This observational fact was early identified (e.g. Zwicky 1942). Dressler (1980) found an increase in the fraction of early-type (ET; elliptical and S0 galaxies) with the local galaxy density and quantified this as the morphology-density relation (MDR). Likewise, a decrease in the number of star forming galaxies

is observed with local density (e.g. Pintos-Castro et al. 2013; Webb et al. 2013; Koyama et al. 2011). These relations evolve over cosmic time: a significant increase in the amount of blue cluster galaxies is observed at  $z > 0.2$  (the Butcher-Oemler effect Butcher & Oemler 1984), as with the cluster star formation (SF) and AGN activity (e.g. Haines et al. 2009; Martini et al. 2013). Elbaz et al. (2007) studied the SF-density relation using deep *Spitzer* observations of the GOODS field, witnessing a vigorous SF activity in the centres of groups at  $z \sim 1$ , which suggests a reversal of the SF-density relation. Tran et al. (2010) found a dramatic increase in the fraction of SF galaxies in a *Spitzer*-selected cluster at  $z \sim 1.62$ , CIG J0218.3-0501, which grew by a factor of three from the lowest to the highest galaxy density regions. This evidence has also been supported by simulations

<sup>★</sup> The catalogues are only available at the CDS via anonymous ftp to [cdsarc.u-strasbg.fr](http://cdsarc.u-strasbg.fr) (130.79.128.5) or via <http://cdsarc.u-strasbg.fr/viz-bin/qcat?J/A+A/592/A108>

from Tonnesen & Cen (2014). However, there is some controversy since Ziparo et al. (2014) find no clear evidence of this type of reversal when studying the evolution of the SF-density relation in the ECFDS and GOODS fields up to  $z \sim 1.6$ .

The correlation of the morphology and/or SF activity of the clusters' galaxies with the local density (as traced by the local galaxy density or dark matter density) can provide clues to the stage of infall at which galaxies experience the bulk of their transformations. Hence, it is important to perform wide-area studies in clusters that span a range of redshifts.

Holden et al. (2007) performed a morphological study of 674 spectroscopically confirmed cluster galaxies from five massive clusters in the redshift range  $z = 0.023$  to 0.83 using *Hubble* Space Telescope (HST) imaging. They performed the analysis using both a luminosity-limited sample (up to  $M_V < M_V^* + 1$ ) and a mass-selected sample (down to  $10^{10.6} M_\odot$ ) to avoid biases owing to changes in the  $M/L$  relation that were related to changes in the star formation rate (SFR). For the luminosity-selected sample, the authors find an increasing fraction of ET galaxies with the local density. This is observed in all the studied clusters, although there is a clear trend of decreasing the fraction of ET galaxies with redshift, in agreement with previous studies (e.g. Postman et al. 2005). When studying the mass-selected sample, they found that the MDR still exists, but shows a lower slope. However, no substantial variation of the slope with redshift was found, which is consistent with no evolution over a period of 7 Gyr. The authors concluded that the redshift evolution of the MDR observed in luminosity-selected samples should be driven by galaxies with stellar masses below  $10^{10.6} M_\odot$ .

Nantais et al. (2013) performed a luminosity-limited morphological study of 124 spectroscopically confirmed members of the cluster RX J1052.7-1357 at redshift 0.84. using HST *riz* ACS imaging. The authors derived the morphology of the galaxies using a parametric method (Sérsic index) and separated their sample into ET and late-type (LT; spirals) categories, and a third class that encompasses peculiar (e.g. galaxies with a nucleus bluer than the outer regions), compact, and merging objects (hereafter referred as PEC). They found that the global percentage of ET galaxies is 47%, about 2.8 times higher than the field. They traced the dependency of morphology on the local dark-matter density (DMD), defining three DMD ranges: low (LDMD), intermediate (IDMD), and high (HDMD). In the LDMD environment, the percentage of ET galaxies is 27% (approximately 1.5 times the value of  $z \sim 0.9$  field and similar to groups at the same redshift), the percentage of LT galaxies 19% (lower than field, 31%), and finally that of PEC galaxies is 53%, similar to field values. In the IDMD environment, the percentage of ET galaxies rises to 61%, that of LT galaxies decreases only very slightly to 16%, but the fraction of PEC objects goes down by half, to 23%. Finally, in the HDMD medium, the amount of ET galaxies increases to 71%, no LT galaxies are found, but the percentage of PEC galaxies is roughly maintained at 21%. The authors suggest that in the IDMD environment, the preferred mechanism is the direct transformation of PEC galaxies into ET ones, rather than from PEC to LT and then to ET. In the transition from IDMD to HDMD environment, LT galaxies disappear, transforming into ET ones. Nevertheless, this last result is less robust owing to the low-number statistics and the fact that, depending on the orbit of the galaxy, the region where the bulk of transformations takes place is not necessarily that in which the galaxy is observed.

The vast majority of studies of the morphology of cluster galaxies are carried out with HST imaging, specially at intermediate and high redshift, owing to the high imaging resolution and

depth required. Parametric and/or visual classification methods are customarily used. In this paper, we attempt to perform a morphological study of an intermediate redshift cluster using images from a ground-based telescope. Huertas-Company et al. (2009a) performed a morphological study of galaxies in a sample of nine rich intermediate redshift clusters in the range  $0.4 < z < 0.6$  that were observed with the CFHT MegaCam in the *griz*-bands up to a cluster-centric distance of some 5 Mpc. Selecting the cluster candidates by photometric redshifts, the authors determined a broad morphological class (early/late) by means of the galSVM code (Huertas-Company et al. 2008, for a short description see Sect. 3) for nearly 4000 objects. The agreement between this ground-based classification and that derived from HST data is better than 90%. When considering the whole sample, they find a clear correlation between morphology and local density with early-type galaxies dominating the densest regions. This correlation holds not only in the central region but also in the cluster outskirts, suggesting that the morphological evolution is mainly driven by the local environment through galaxy-galaxy interactions, which are independent of cluster properties. Here we apply the same approach to our data. As part of the GLACE project (Sánchez-Portal et al. 2015), an OSIRIS/GTC program to study the evolution of emission-line galaxies in clusters, we perform a complete study of the young massive galaxy cluster RXJ 1257.2+4738 (hereafter referred to as RXJ 1257) at  $z = 0.866$ . The first part of the work, reported in Pintos-Castro et al. (2013, hereafter Paper I), included the compilation of a multi-wavelength dataset to build a reliable sample of cluster members, and the study of the population of far-infrared (FIR) emitters, to analyse the relation of the environment with the star formation activity and other galaxy properties, such as the stellar mass. In the second part, described in this paper, we have exploited the OSIRIS/GTC broad-band imaging to perform, using non-parametric methods, a morphological classification of the full cluster sample and investigate the relation between the morphology of the galaxies and their cluster environment. The third part, addressed in Pintos-Castro et al. (in prep., hereafter Paper III), will describe the [O II] TF/OSIRIS observations, including a catalogue of fainter star-forming galaxies formed by the RXJ 1257 [O II]-emitters, with the aim of building a deeper picture of the star formation activity in the cluster, and taking the opportunity to compare both [O II] and FIR star formation estimators.

This paper is organised as follows: in Sect. 2, we give a summary of the observations used in this study, in Sect. 3, we present a detailed description of the morphological classification method employed: the galSVM code, and in Sect. 4, we present the results obtained with this classification technique using ground-based observations. The physical properties of the different morphological types are described in Sect. 5, and the specific discussion about the explanations for the finding of a large optically blue early-type population are summarised in Sect. 6. The investigation of the morphology-density relation in the RXJ 1257 cluster is discussed in Sect. 7, and a summary of the essential results is provided in Sect. 8. Throughout this paper, we assume a Universe with  $H_0 = 70 \text{ km s}^{-1} \text{ Mpc}^{-1}$ ,  $\Omega_{\Lambda,0} = 0.7$ , and  $\Omega_{m,0} = 0.3$ . Magnitudes are listed in the AB system (Oke & Gunn 1983).

## 2. Data

Most of the data used in this paper were extensively described in Paper I, with the exception of the [O II] data that will be fully detailed in Paper III. In this section, we summarize the data that concern to the morphological analysis.

## 2.1. Optical broadband imaging

Broadband imaging with SDSS  $g'r'i'z'$  filters was obtained using the OSIRIS (Cepa et al. 2003) instrument at the 10.4 m GTC telescope, as part of a large ESO/GTC program (ID. 186.A-2012, P.I. M. Sánchez-Portal). The data were gathered during two dark nights under photometric conditions, with a seeing below  $1.1''$ . Observations were planned to place the cluster centre at the CCD2, placing a bright star in the gap between both CCDs (see Fig. 1). Therefore, the three position dithering pattern was designed so as not to cover the gap. Total on-source exposure times for  $g'r'i'z'$  were 180 s, 450 s, 450 s, and 2000 s, respectively. The reduction process was performed following standard IRAF<sup>1</sup> procedures. Individual frames were bias-subtracted, flat-fielded, fringing-corrected (only for  $z'$ ), aligned, and coadded to produce deep mosaics. Astrometry was performed using the SDSS DR6, obtaining an accuracy better than  $0.17''$ . The flux calibration was made by comparing observations of photometric standard stars with the SDSS DR6.

Source detection and photometry were carried out using SExtractor (Bertin & Arnouts 1996). The total flux for each source was estimated with the FLUX\_AUTO parameter, while the FLUX\_APER was used for calculating optical colours. Since we use the  $r'$ -band to estimate the morphological parameters, we used this image as a reference for object detection in the SExtractor dual mode. The final optical catalogue includes 1894 sources with completeness levels at 50% of 25.0, 24.3, 24.2, and 23.4 mag for  $g'r'i'z'$ , respectively. A final check of our photometry was performed against that from Ulmer et al. (2009). To that end, we compared the distributions of galaxies in the  $i' - z'$  vs.  $i'$  colour–magnitude diagram (a direct comparison of individual galaxies was not possible since the referred authors did not publish a source catalogue). Both distributions were found to be highly compatible in both magnitude and colour range, and also in the relative source counts in each colour and magnitude bin.

## 2.2. OSIRIS/TF imaging: [O II]

OSIRIS [O II]  $\lambda 3727$  observations were carried out as part of the same large ESO/GTC program, during semesters 11A, 12A, and 13A, under photometric and non-photometric nights. We designed the observations to cover the spectral range 6884–7114 Å (to scan a velocity field of at least  $\pm 3000$  km s<sup>-1</sup>) with 24 scan steps spaced 10 Å, with a total on-source exposure time of 18 h. At each TF tuning, three individual exposures of 900 s without dithering pattern were taken (to avoid wavelength shifts and saturation problems). To carry out the TF data flux calibration we obtained long-slit spectroscopy of two stars in the RXJ 1257 cluster field with the OSIRIS instrument. These observations were carried out under photometric conditions. For each star, one spectrum of 1500 s was taken using the R1000R grism with a slit of  $2.5''$  width and  $8.67''$  length in the spatial direction. For more details on the reduction and calibration processes of the [O II] TF data see Sánchez-Portal et al. (2015) and Paper III.

After the data reduction, we have 4478 pseudo-spectra available in the RXJ 1257 field to select the [O II] cluster emitters. The process for selecting the [O II] cluster members includes: (i) automatic classification by the definition of the existence of

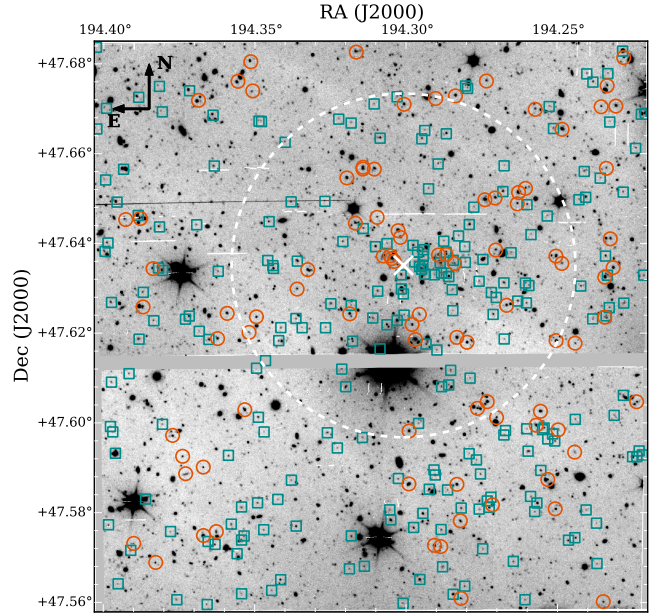


**Fig. 1.** Projected spatial distribution for the cluster galaxies, the morphological classified (orange circles) and unclassified (cyan squares) sub-samples, represented over the  $r'$ -band image. The white cross and dashed white circle are the cluster centre and virial radius, respectively.

an emission line in the pseudo-spectra based on a signal-to-noise (S/N) criterion (1080 emission-line galaxy (ELG) candidates); (ii) visual inspection of the pseudo-spectra automatically classified (271 ELG candidates); (iii) visual inspection of the galaxy stamps in each TF image (161 ELGs); (iv) rejection of interlopers using the colour–colour diagram (118 [O II]-emitters); and, (v) constraint of the line-of-sight velocity ( $v_{\text{LOS}}$ ) covered over the entire OSIRIS field-of-view (87 [O II]-emitters within a complete  $v_{\text{LOS}}$ ).

## 2.3. Multi-wavelength catalogue

To define a reliable sample of cluster members, the first step is to build a multi-wavelength optical-to-NIR catalogue. As already explained in Paper I, we cross-matched the optical catalogue with  $J$ -band and IRAC four channel catalogues, using the nearest-neighbour technique that follows Geach et al. (2006) and the de Ruiter et al. (1977) methodology. This catalogue was used to estimate photometric redshifts by fitting the spectral energy distribution (SED) of each source. The stellar part of the spectrum was fitted with Bruzual & Charlot (2003) templates using the LePhare code (Ilbert et al. 2006). The galaxies' cluster membership was determined through Monte Carlo simulations: (i) we created 600 mock catalogues by randomly varying every band flux within its error; (ii) we fitted the SED with LePhare, obtaining both a photometric redshift distribution (with 600 values) for each source and 600 photometric redshift distributions for the cluster; (iii) with the cluster distribution, we defined an initial cluster redshift range, then we considered as cluster candidates those sources that satisfied that  $1\sigma$  width centred at the central position of the best-fitted Gaussian function to the  $z_{\text{PHOT}}$  distribution is completely included within this range; and, (iv) finally the sample was constrained, redefining the cluster photometric redshift range with the accuracy ( $\sigma_{\Delta z/1+z} = 0.094$  at the cluster redshift), obtaining 271 galaxies with photometric redshift

<sup>1</sup> IRAF is distributed by the National Optical Astronomy Observatory, which is operated by the Association of Universities for the Research in Astronomy, Inc., under a cooperative agreement with the National Science Foundation (<http://iraf.noao.edu/>).

between 0.79 and 0.98. For more details on the SED-fitting and cluster sample definition, see Paper I.

The photometric cluster sample thus defined, along with a small spectroscopic sample (Ulmer et al. 2009), yielded to a cluster sample of  $271 + 21 = 292$  galaxies. We merged this first cluster catalogue, using the nearest neighbour technique with a maximum error radii of  $1.5''$ , with the [O II]-emitters sample  $\nu_{\text{LoS}}$  complete, and obtained a final cluster catalogue of 315 members. The FIR data, already exploited in the first paper, was again matched with this updated cluster catalogue, as explained in Pintos-Castro et al. (2013). Therefore, the final catalogue of 315 cluster galaxies used in this work includes: 21 spec-z, 87 TF-z with [O II] emission, and 207 photo-z. This sample also includes 37 FIR emitters.

### 3. Morphological classification: methodology

Accomplishing the morphological classification of galaxies in the RXJ 1257 cluster is a complex task. First, because of its high redshift distribution and, second, since up to now, high-resolution optical data have been unavailable. Therefore, the visual classification and methods based on galaxy decomposition and fitting were discarded from the beginning, and we instead decided to test the non-parametric methods.

In this work we used the galSVM code<sup>2</sup> (Huertas-Company et al. 2008). This is a publicly available code that works in IDL, and uses the freely available library libSVM (Chang & Lin 2011) to perform morphological classification in an automated way using support vector machines (SVM)<sup>3</sup>. This code can use a number of parameters simultaneously and non-linear boundaries between them to classify galaxies. Moreover, it has already been tested on high-redshift and low-resolution samples of galaxies (e.g. Huertas-Company et al. 2008, 2009b, 2011, 2016; Pović et al. 2013, and references therein), obtaining reliable classifications.

We followed the standard galSVM procedure, as described in Huertas-Company et al. (2008). The code uses a training set of local galaxies with known visual morphology to train the SVM, which is then applied to classify the real dataset (RXJ 1257 cluster galaxies in our case). galSVM creates simulated galaxies from the local sample ones: galaxies that are redshifted and scaled in luminosity to match the magnitude and redshift distributions of the studied sample, re-sampled with the RXJ 1257  $r'$  broadband pixel scale, and dropped in a real cluster image background. A set of morphological parameters is then measured on the local dataset of simulated galaxies and afterwards on the cluster sample, and used to train the vector machine. galSVM code analyses the simulated sample by comparing the obtained morphological parameters and the original visual classification and performs a weighted distribution of the morphological type for the real cluster sample. During this last step, the support vector-based learning machine is trained with a fraction of the simulated sample so that, when repeating the process through Monte Carlo simulations, the sub-sample of the simulated sample is different in each run. From each Monte Carlo simulation, we obtain one probability with values between 0 and 1, for every galaxy to be ET ( $p_{\text{ET}}$ ). The final probability was obtained as average of all previous probabilities. The probability for the source to be LT is then  $p_{\text{LT}} = 1 - p_{\text{ET}}$ . We assumed that there is no significant change in galaxy properties between the

local and high-redshift samples, although brightness dimming is taken into account. This assumption might be strong for our redshift  $\sim 0.9$ , but to minimize the effect we classified galaxies into two broad morphological types (ET and LT), and for each Monte Carlo run we forced galSVM to select the same number of ET and LT local galaxies from the training sample. Finally, in our two-type classification the ETs include elliptical (E), lenticular (S0), and S0a galaxies, while the LT group consists of spirals and irregulars.

#### 3.1. Description of the measured morphological parameters

We measured six morphological parameters, commonly used in the non-parametric methods. In the following, we provide a brief description for each of them. In all definitions, when necessary, the galaxy centre is determined by minimizing the asymmetry index, while the total flux is defined as the one contained within 1.5 times the Petrosian radius ( $r_p$ , measured by SExtractor; see Huertas-Company et al. 2008).

- *Abraham concentration index* ( $C$ , Abraham et al. 1996). This is defined as the ratio between the fluxes of two isophotes. In our case the inner and outer isophotes contain 30% and 90% of the total flux, respectively:

$$C = \frac{\sum_{i,j \in E(0.3)} I(i,j)}{\sum_{i,j \in E(0.9)} I(i,j)}, \quad (1)$$

where  $I(i, j)$  is the original image pixel index.

- *Bershady-Conselice concentration index* ( $C_{\text{BC}}$ , Bershady et al. 2000). This parameter is defined as the ratio between the circular radii containing 80% and 20% of the total flux:

$$C_{\text{BC}} = 5 \log \frac{r_{80}}{r_{20}}. \quad (2)$$

- *Gini coefficient* (GINI, Abraham et al. 2003; Lotz et al. 2004). This is a statistic parameter based on the Lorentz curve that presents the cumulative distribution function of a galaxy's pixel  $i$  values:

$$\text{GINI} = \frac{1}{|\bar{X}|n(n-1)} \sum_i^n (2i - n - 1)|X_i|, \quad (3)$$

where  $n$  is a total number of pixels in a galaxy,  $X_i$  the pixel flux value, and  $|\bar{X}|$  the mean over all pixel flux values. This is another type of concentration index and usually correlates with  $C$  and  $C_{\text{BC}}$ . However, unlike the previous concentration indexes, it can distinguish between galaxies with shallow light profiles and those with the light concentrated in a few pixels, but outside the galaxy centre.

- *Asymmetry* ( $A$ , Abraham et al. 1996; Conselice et al. 2000). This measures the degree to which the light of the galaxy is rotationally symmetric. It is quantified by subtracting the galaxy rotated by  $180^\circ$  from the original image:

$$A = \frac{1}{2} \left( \frac{\sum (|I(i,j) - I_{180}(i,j)|)}{\sum I(i,j)} - \frac{\sum (|B(i,j) - B_{180}(i,j)|)}{\sum I(i,j)} \right), \quad (4)$$

<sup>2</sup> <http://gepicom04.obspm.fr/galSVM/Home.html>

<sup>3</sup> Group of supervised learning methods that can be applied to classification or regression.

where  $I$  is the flux in the original image,  $B$  is the flux in the background image, while the subindex 180 refers to the original and background images rotated by  $180^\circ$  around the central pixel of the galaxy.

- *Smoothness or clumpiness* ( $S$ , [Conselice et al. 2003](#)). This quantifies the degree of small-scale structure of the galaxy. The image is smoothed with a box of width  $0.25 r_p$  and then subtracted from the original image:

$$S = \frac{1}{2} \left( \frac{\sum (|I(i, j) - I_S(i, j)|)}{\sum I(i, j)} - \frac{\sum (|B(i, j) - B_S(i, j)|)}{\sum I(i, j)} \right), \quad (5)$$

where  $I$  and  $B$  are defined as in the case of  $A$ , while the subindex  $S$  refers to the smoothed image. The resulting image provides information about possible clumpy regions.

- $M_{20}$  *moment of light* ([Lotz et al. 2004](#)). It is defined as a normalized second-order moment of the 20% brightest pixels of the galaxy:

$$M_{20} = \log \frac{\sum_{f_i < 0.2 f_{\text{tot}}} M_i}{M_{\text{tot}}}, \quad (6)$$

where  $f_i$  is the flux at the  $i$  pixel and  $M_{\text{tot}}$  the total second-order moment, defined as the flux in each pixel  $(x_i, y_i)$  multiplied by the squared distance to the centre of the galaxy  $(x_c, y_c)$  and summed over all the galaxy pixels assigned by the segmentation map:

$$M_{\text{tot}} = \sum_i^n f_i [(x_i - x_c)^2 + (y_i - y_c)^2]. \quad (7)$$

This parameter can trace the spatial distribution of any bright core, bar, spiral arm, and off-centre star cluster.

### 3.2. Description of the training set of local galaxies and related methodology

In this work, we used a sample of 4000 local galaxies classified visually by [Nair & Abraham \(2010\)](#), using the  $g$  and  $r$ -bands. The galaxies have redshifts distributed in the range  $0.01 \leq z \leq 0.1$ , and were drawn from the SDSS Data Release 4 (DR4) down to an apparent extinction-corrected magnitude of  $g < 16$ . For all galaxies, we provided as an input information for galSVM a catalogue that includes redshift, magnitude, morphological type, and half-light radius, plus original, PSF, and mask images. The build of the training set of local galaxies is described in [Pović et al. \(2013\)](#). The galaxies were selected randomly out of  $\sim 14\,000$  sources contained in the [Nair & Abraham \(2010\)](#) catalogue, making sure that the selected sub-sample is representative in terms of general properties of the whole data set:  $g$ -band magnitude, redshift,  $g-r$  colour, morphological classification, and inclination in the case of the late-type galaxies. On the other hand, the number of local galaxies is selected as a compromise between the computing time and the classification accuracy, since the computing time to train the SVM through the galSVM code is totally dependent and sensitive to the size of the training data set ([Huertas-Company et al. 2008, 2009a](#)). Figure 2 shows the redshift,  $g$ -band magnitude, and morphological classification (T-Type in [Nair & Abraham \(2010\)](#) classification) distributions of the selected local sample. As can be seen from the

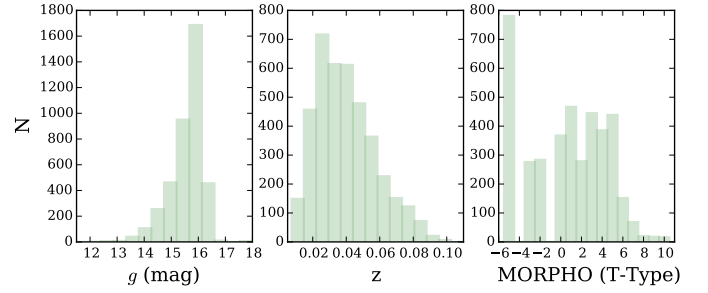


**Fig. 2.** Distributions of the  $g$ -band magnitude (*left*), redshift (*centre*), and morphological type (*right*) for the training sample of 4000 local galaxies.

T-Type histogram, the selected sample spans all ranges of morphology, from elliptical to irregular galaxies.

This local sample of 4000 galaxies was moved to the appropriate redshift, luminosity, and image quality for the RXJ 1257 field. To that purpose, galSVM requires, along with the image characteristics (pixel scale =  $0.254'' \text{ px}^{-1}$ ,  $FWHM = 1.1''$ , gain = 0.95, saturation level = 30 000), the apparent magnitude and redshift distributions of the cluster sources. For every local galaxy stamp, galSVM generates a random pair of magnitude and redshift values, with a probability distribution that matches that of the cluster galaxies. Moreover, each simulated local galaxy is re-sampled with the corresponding pixel scale and convolved with the PSF to match the same spatial resolution.

In the subsequent step, we dropped the simulated galaxies into the background of the RXJ 1257 image by randomly selecting locations free of objects (by means of the NUMBER SExtractor parameter and the segmentation image). We then used the SExtractor mask image to eliminate nearby objects.

Finally, we measured the simulated galaxies to estimate the set of morphological parameters listed in Sect. 3.1 and the ellipticity, as determined by SExtractor. We used these seven parameters simultaneously to train the SVM. The particular set of parameters used to obtain the morphological classification was tested in [Huertas-Company et al. \(2008, 2009a\)](#) and [Pović et al. \(2012, 2013\)](#).

### 3.3. Methodology applied on the RXJ 1257 galaxies

Using galSVM code, we measured the same set of seven morphological parameters of the RXJ 1257 members, as in the case of simulated local galaxies. We used the  $r'$ -band image to perform the classification of cluster galaxies since it shows the highest S/N. To take care of the  $k$ -correction effect when simulating local galaxies, SDSS  $u$ -band images correspond to the selected band at the redshift of our cluster. Since the filter efficiency for the SDSS  $u$  band is very poor and much lower than that for  $g$ ,  $r$ , and  $i$ -bands ([Gunn et al. 1998](#)), and taking into account that the aim of our work is not to deal with the fine morphology but to classify galaxies into only two broad morphological groups (early- or late-type), we used the  $g$ -band images instead of  $u$ - (see [Pović et al. 2015](#)). Support vector-based learning machines were trained with a sample of 3000 out of 4000 initial simulated local galaxies. This number of galaxies was selected to be high, but still low enough to include different galaxies from one Monte Carlo run to another. As a result of an empirical trade-off between computing time and accuracy tested with 10, 15, and 20 Monte Carlo simulations, we repeated the classification

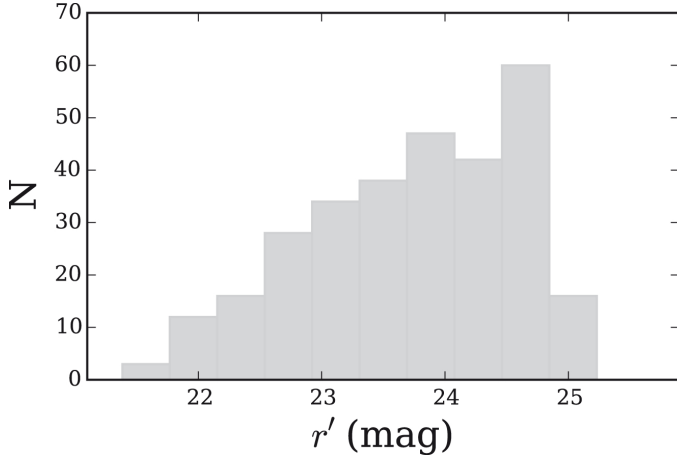


**Fig. 3.** Histogram of the  $r'$  magnitude that corresponds to the full cluster sample.

of our cluster galaxies through 15 independent Monte Carlo runs. As mentioned above, in each run we use a different combination of 3000 local galaxies out of 4000 initially selected, increasing therefore the accuracy of our classification. From each Monte Carlo simulation, we obtained the probability for every galaxy to be ET, and measured the final probability as the average of these probability values, and its error as the standard deviation of the probability distribution.

galSVM code is optimised to classify faint galaxies. This means that, if using a wide range of magnitudes, the fraction of misclassified bright objects could be significant (Huertas-Company et al. 2008). In our case, the RXJ 1257 cluster sample is dominated by faint sources, as shown by the shape of the magnitude distribution in Fig. 3, where 49% of the sources are fainter than  $r' = 24$ . Therefore, to avoid this effect, we performed the morphological classification within five magnitude bins:  $m \leq 22.5$ ,  $22.5 < m \leq 23.5$ ,  $23.5 < m \leq 24$ ,  $24 < m \leq 24.5$ , and  $24.5 < m \leq 25$ . The redshift and magnitude distributions that correspond to each magnitude bin are shown in Fig. 4. These are the distributions that we used for simulating the local galaxy sample. We also tested the morphological classification when dealing with increasing magnitude cuts:  $m \leq 22.5$ ,  $m \leq 23.5$ ,  $m \leq 24$ ,  $m \leq 24.5$ , and  $m \leq 25$ , but we found that, in some cases, fainter objects were slightly better classified (with higher probabilities) using smaller magnitude bins.

### 3.4. Estimation of errors of the morphological parameters

The galSVM code does not estimate uncertainties of the measured morphological parameters. The only output error estimate is the standard deviation of the probabilities determined in each Monte Carlo simulation. To get an idea of the errors associated with the morphological parameters that have been used to perform the classification with the galSVM code, we proceeded as follows: (i) we estimated the  $r'$ -band image noise; (ii) we generated 100 mock images by randomly varying every pixel counts within a Gaussian of sigma value equal to the image noise; (iii) we measured the morphological parameters used in each mock image; (iv) for each galaxy we obtained a distribution of each morphological parameter and we associated its standard deviation with its error. Figure 5 shows the distributions of percentage errors for the  $C$ ,  $C_{BC}$ , GINI, and  $A$  morphological

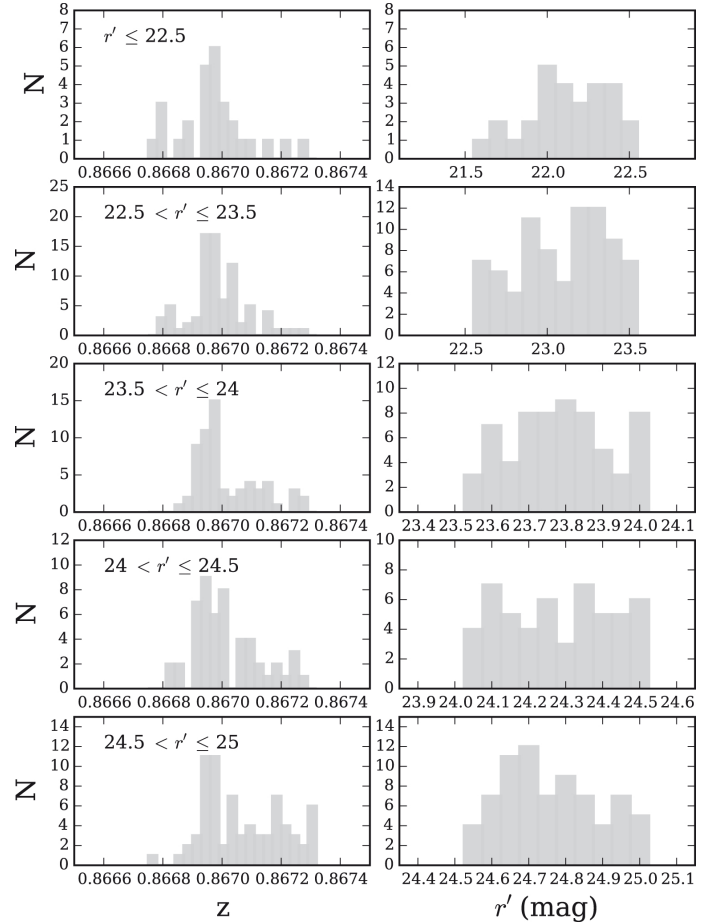


**Fig. 4.** Distributions of redshift (left) and magnitude (right) for each of the bins used to run the galSVM code.

parameters obtained for the cluster galaxies morphologically classified. We observe in this figure that, with the exception of the error associated to the  $C_{BC}$  parameter of a set of six galaxies, the error values are lower than 5%, being around 1% for the concentration indexes and around 3% for the asymmetry. The M20 parameter was omitted in this figure since it remains invariant under image-noise variations.

## 4. Morphological classification: results

Before discussing the properties of the classified galaxies, it is necessary to define the limits within which we could consider the morphological classification to be reliable. The probability that a galaxy is ET (or LT) represents a measurement of the accuracy of the morphological classification. It has been shown that there is a clear correlation between the  $p_{ET}$  probability threshold and the number of correct identifications: accuracy clearly increases when the considered probability is higher. Huertas-Company et al. (2009b) compared WIRCam data at the Canada France Hawaii Telescope with HST/ACS observations, and found that objects with  $p_{ET}$  probabilities between 0.5 and 0.6 have mean accuracy of around 58%, while objects with probabilities greater than 0.8 are classified as ET with an accuracy of nearly 90%. Owing to the unavailability of higher-resolution and comparable morphological classifications, we analysed probability distributions and standard diagnostic diagrams to establish the probability boundaries under which our morphology is reliable. We also tested the physical properties of classified sources.

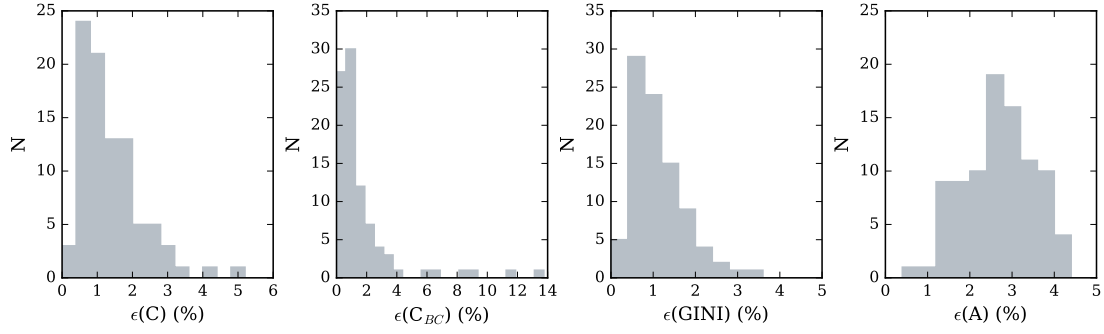


**Fig. 5.** Distributions of the percentage errors associated to  $C$ ,  $C_{BC}$ , GINI, and  $A$  morphological parameters.

Figure 6 shows the obtained average probability distributions and their errors in six analysed magnitude bins. As already mentioned above, the errors were estimated as the standard deviation of the probabilities obtained in the 15 Monte Carlo simulations. In this figure, two trends can be observed: on the one hand, the brightest galaxies are mainly classified as ETs, as expected in a cluster, while those classified as LTs show fainter magnitudes; on the other hand, towards higher magnitude bins to distinguish between both types becomes more complicated, resulting in a peak of probability distribution around 0.5. For all magnitude bins, the probability errors are kept mostly below 0.1.

We tested a set of probability limits for each magnitude bin, applying more restrictive values for fainter magnitudes, and therefore analysed standard morphological, colour-magnitude, and colour-stellar mass diagrams. When defining the probability thresholds, we took into account the probability error, i.e. a galaxy should satisfy the condition  $p_{ET} - \epsilon(p_{ET}) \geq p_{th}^{ET}$  to be classified as a trustworthy ET galaxy, where  $p_{th}^{ET}$  is the probability threshold to classify ET galaxies in a given magnitude bin, while  $\epsilon(p_{ET})$  is the corresponding error. Figure 7 shows five of the standard morphological diagnostic diagrams. None of these diagrams represents smoothness since this parameter is extremely sensitive to spatial resolution, data depth, and noise, as shown in Pović et al. (2015), and for most of our galaxies we obtained non-valid values. As shown in Fig. 7, only using  $M_{20}$ ,  $C_{BC}$ , and  $C$  parameters one can roughly classify ET and LT galaxies.

In general, the individual morphological diagnostic diagrams do not segregate clearly between both types. Nevertheless, for the LT galaxies, we observed that a probability threshold of 0.3 for the faintest galaxies ( $r' > 23$  mag, represented in dark blue in Fig. 7) is acceptable for placing the majority of galaxies in the expected position in the morphological diagnostic diagrams (e.g. Abraham et al. 1996; Lotz et al. 2004). Therefore, we selected the LT sample including the galaxies that satisfied  $p_{ET} + \epsilon(p_{ET}) \leq 0.4$  for the brightest galaxies, i.e. with magnitude  $r' \leq 23$  mag, and  $p_{ET} + \epsilon(p_{ET}) \leq 0.3$  for the fainter ones. For the ET sample, the brightest galaxies with  $r' \leq 23$  mag were clearly classified when  $p_{ET} - \epsilon(p_{ET}) \geq 0.6$ , as shown by the probability distributions and the morphological diagnostic diagrams (see Figs. 6 and 7). In contrast, we observed that fainter galaxies, classified as ET, tend to blend into the LT region in the morphological diagnostic diagrams. For faint galaxies the information from the galactic disc can easily be lost, increasing the number of ET misclassified galaxies owing to contamination of LT ones. Therefore, we established two more restrictive probability thresholds:  $p_{ET} - \epsilon(p_{ET}) \geq 0.7$  for  $23 < r' \leq 24$ , and  $p_{ET} - \epsilon(p_{ET}) \geq 0.9$  for the faintest galaxies. The probability classification thresholds for both ET and LT types are summarized

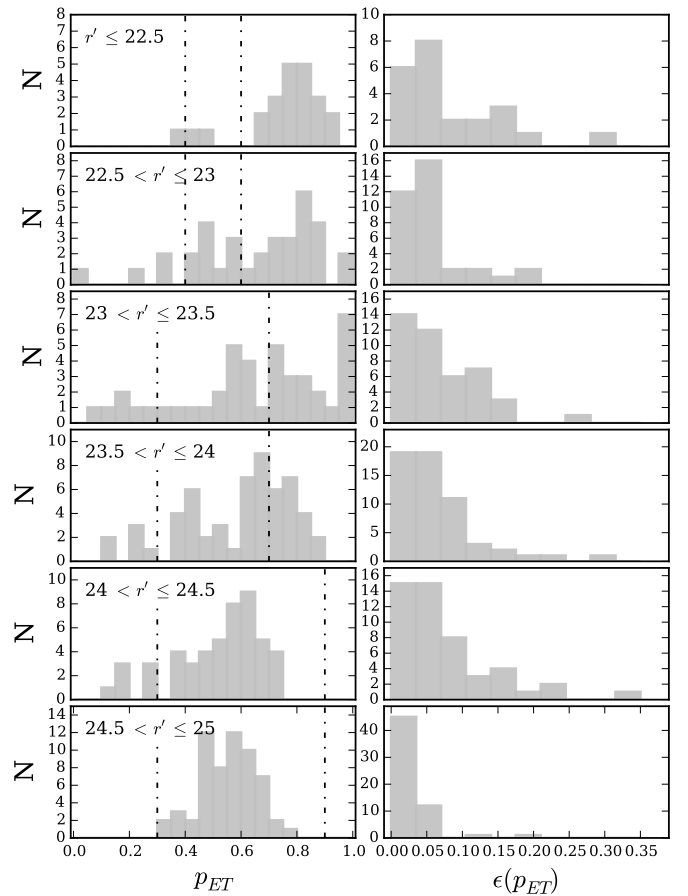


**Fig. 6.** Distribution of the  $p_{ET}$  (left) and of their errors (right) for each analysed bin of magnitude. The dot-dashed vertical lines indicate the final probability boundaries we considered for the separation between morphological types, ET, and LT galaxies, as indicated in Table 1.

in Table 1 and plotted as dot-dashed vertical in Fig. 6. In total, we obtained the reliable classification for 30% of all cluster members.

Figure 8 shows the distributions of  $r'$  magnitude, stellar mass, size, local galaxy density, and distance to the cluster centre of the whole cluster sample and of the classified one (summarized in Table 2). The size was estimated as an area covered by the ellipse used by SExtractor to extract the source. The local galaxy density  $\Sigma_5$  was defined as the inverse of the area that comprises the five nearest neighbours (Tanaka et al. 2005). Our classification is incomplete towards fainter galaxies since all

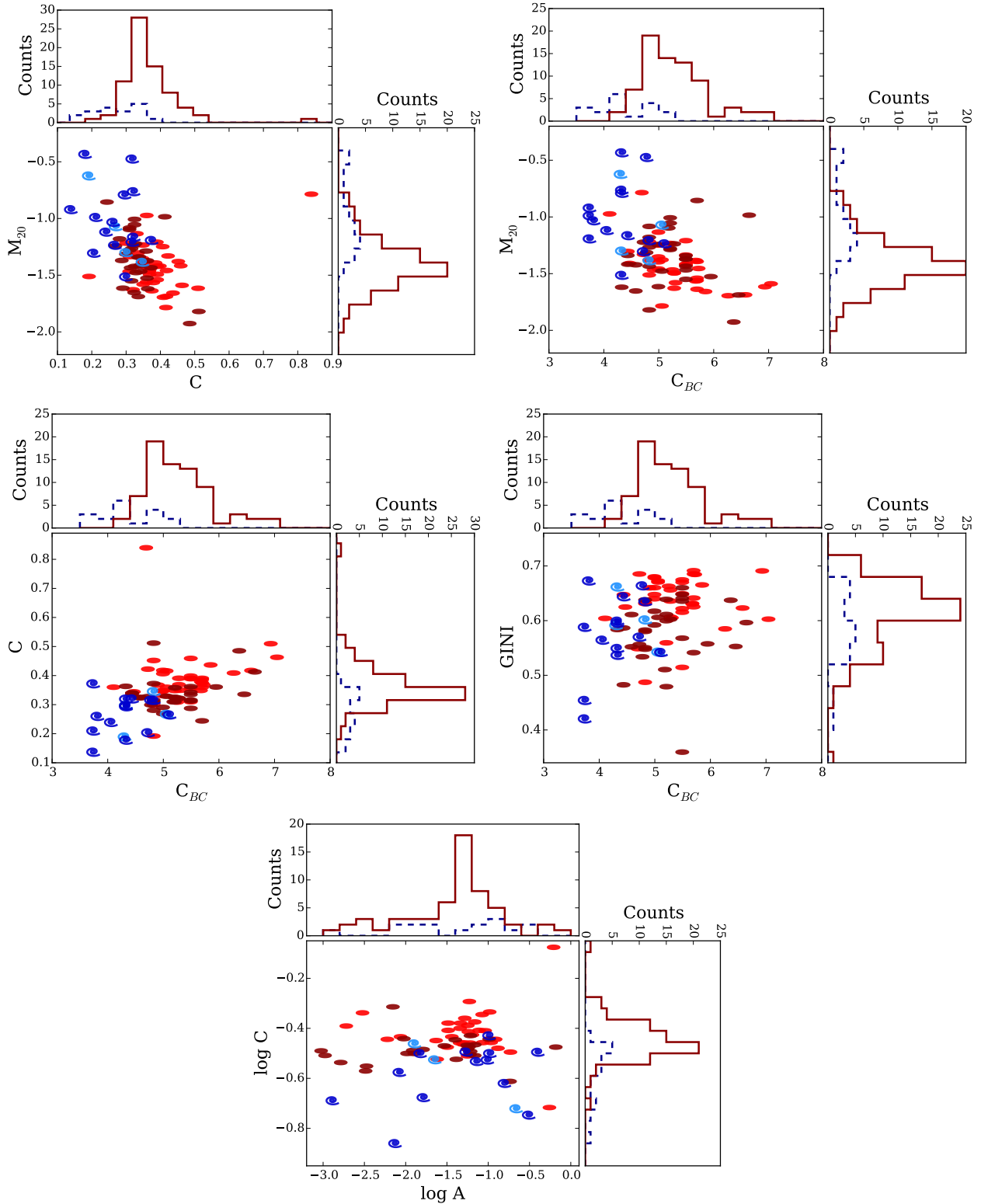


**Fig. 7.** Morphological diagnostic diagrams representing the following relations:  $M_{20}$  (moment of light) vs.  $C$  (Abraham concentration index) (*top left*),  $M_{20}$  vs.  $C_{BC}$  (Bershady-Conselice concentration index) (*top right*),  $C$  vs.  $C_{BC}$  (*centre left*), GINI (Gini coefficient) vs.  $C_{BC}$  (*centre right*), and  $\log C$  vs.  $\log A$  (asymmetry) (*bottom*). Blue spirals represent galaxies classified as LT, and red ellipses as ET, while light and dark colours refer to galaxies fainter and brighter than 23 mag in  $r'$ , respectively. Typical errors of all these parameters are comparable to or lower than the symbols' size. Histograms show the morphological parameter distribution for each type, the red solid line is for ET galaxies and the blue dashed one for LT galaxies.

galaxies fainter than  $r' = 24.5$  failed to be reliably classified (see Tables 1 and 2). Consequently, our sample of classified cluster

members is incomplete in stellar mass, with less massive galaxies remaining unclassified. Nevertheless, both the whole galaxy

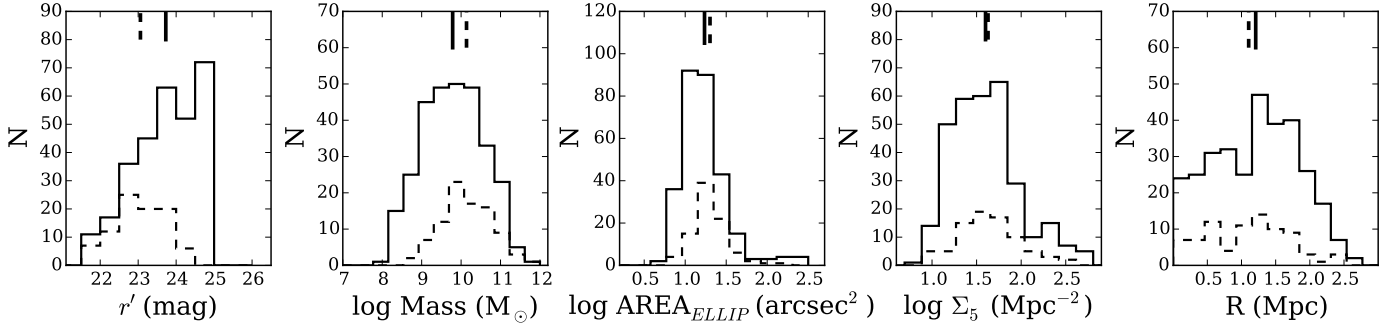


**Fig. 8.** Distributions of the  $r'$  magnitude, stellar mass, size, local galaxy density, and cluster-centric distance. The solid line represents the full cluster sample and the dashed line is the morphologically classified sub-sample. Vertical lines indicate the average value of each distribution.

**Table 1.** galSVM probability threshold for selecting ET and LT galaxies in the analysed  $r'$  magnitude bins.

$r'$ bin	ET	LT
	$p_{\text{ET}} - \varepsilon(p_{\text{ET}})$	$p_{\text{ET}} + \varepsilon(p_{\text{ET}})$
21.5–22.5	$\geq 0.6$	$\leq 0.4$
22.5–23.0	$\geq 0.6$	$\leq 0.4$
23.0–23.5	$\geq 0.7$	$\leq 0.3$
23.5–24.0	$\geq 0.7$	$\leq 0.3$
24.0–24.5	$\geq 0.9$	$\leq 0.3$
24.5–25.0	$\geq 0.9$	$\leq 0.3$

sample and the classified subsample appear to be consistent in terms of other properties, such as size, age, and morphological parameters. In relation to the environment, neither the local galaxy density nor the cluster-centric distance distributions show differences between the whole and classified samples. In fact, applying the Kolmogorov-Smirnov (e.g. [Fasano & Franceschini 1987](#)) statistics, we obtained high p-values (56 and 36% for local density and cluster-centric distance, respectively), which confirmed the hypothesis that both distributions are drawn from the same parent population.

Once the probability boundaries were established, we were able to study the physical properties of morphologically classified cluster sample. First, we analysed their optical colours through the  $r' - z'$  vs.  $z'$  colour–magnitude diagram (CMD), shown in Fig. 9. In Fig. 9, we observed a large fraction ( $\sim 64\%$ ) of the ET population that falls in the blue region. This area is expected to be mainly populated by LT galaxies (at the 70–80% level), even though ET galaxies with recent star formation can also be present (e.g. [Deng et al. 2009](#); [Schawinski et al. 2009](#); [Huertas-Company et al. 2010](#)). In our case, 51% of the morphologically classified galaxies showed this behaviour. Owing to the large number of galaxies classified as ET, which presented this unusual blue colour, we decided to make a third morphological group and analyse its properties and dependencies separately. On the basis of the  $r' - z'$  colour bimodal distribution, we draw the line between so-called standard and blue ET galaxies at  $r' - z' = 1.5$  mag (as shown in Fig. 9 by the horizontal dot-dashed line). This threshold was determined as the  $\mu - 2\sigma$  value that corresponds with the Gaussian function fitted to the red part of the  $r' - z'$  distribution. Besides these blue ET galaxies, in this diagram we observed that at least three LT galaxies fall into the red region. The presence of these red LT galaxies in clusters is not surprising, since they could be transition objects, from blue LT to red ET galaxies ([Wolf et al. 2009](#); [Vulcani et al. 2015](#)). The red colour of this LT galaxy could also be caused by the presence of

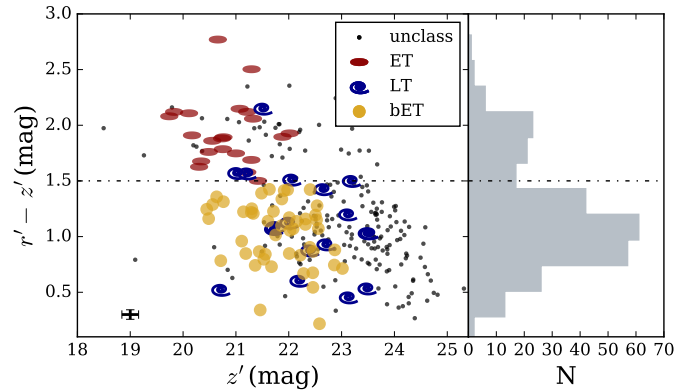


**Fig. 9.** CMD of RXJ 1257 (*left*) and  $r' - z'$  colour distribution (*right*). Symbols are the same as in Fig. 7. Blue spirals represent galaxies classified as LT, red ellipses as ET, and yellow circles are so-called blue ET galaxies. The horizontal dot-dashed line at  $r' - z' = 1.5$  mag is used to separate between the red and blue populations (and, consequently, to differentiate between so-called standard and blue ET galaxies). Small black dots are morphologically unclassified cluster members. The typical error bar is shown in the lower left corner of the plot. In the left panel, the histogram shows the whole cluster sample.

**Table 2.** Number of LT, ET, and blue ET galaxies in each  $r'$  magnitude bin, including the percentage of morphologically classified galaxies.

$r'$ bin	ET	LT	Blue ET	% Classified
21.5–22.5	8	0	11	68
22.5–23.0	6	4	15	69
23.0–23.5	5	3	12	44
23.5–24.0	3	5	12	32
24.0–24.5	0	6	0	12
24.5–25.0	0	0	0	0
Total	22	18	50	30

dust or by a high angle of inclination. Table 2 shows the number of galaxies included in each morphological group and the percentage of well-classified galaxies relative to the total number of cluster members, overall and per magnitude bin.

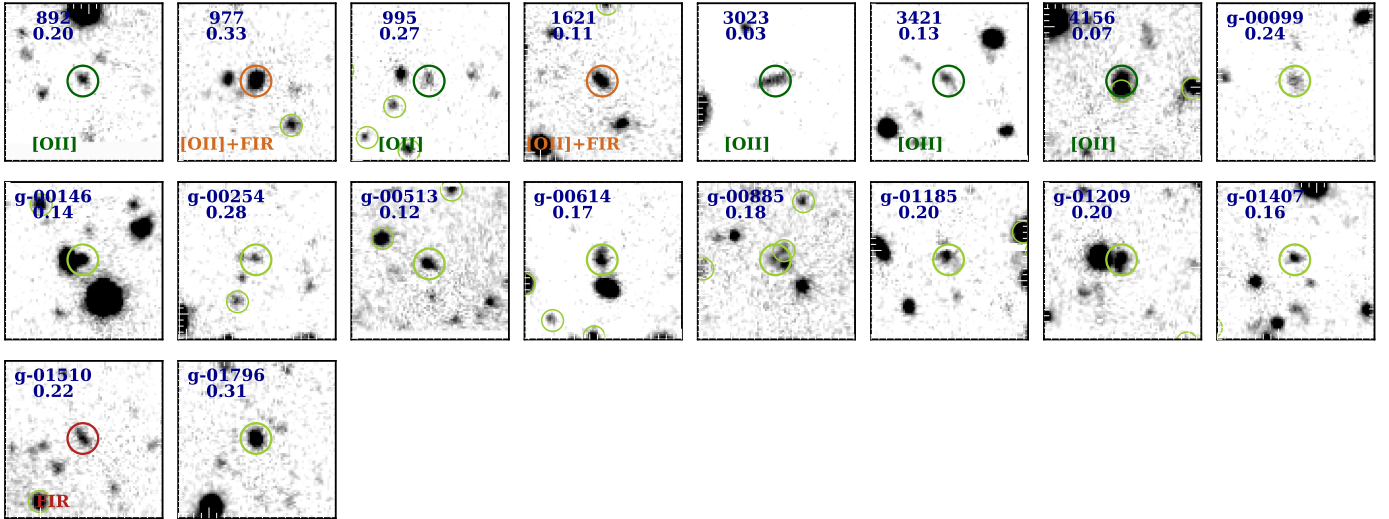


**Fig. 10.** Thumbnails of the galaxies classified as LT, according to the probability thresholds shown in Table 1. Upper labels are the identification name and the probability value, and lower label is, when detected, the emission type. Green circles indicate galaxies considered as cluster members. Central circles mark the classified galaxy, with the colour indicating the type of emission (dark green, red, and orange for [O II], FIR, and both, respectively). Each thumbnail is  $10 \text{ arcsec}^2$  and the colour scale is equal in every image.

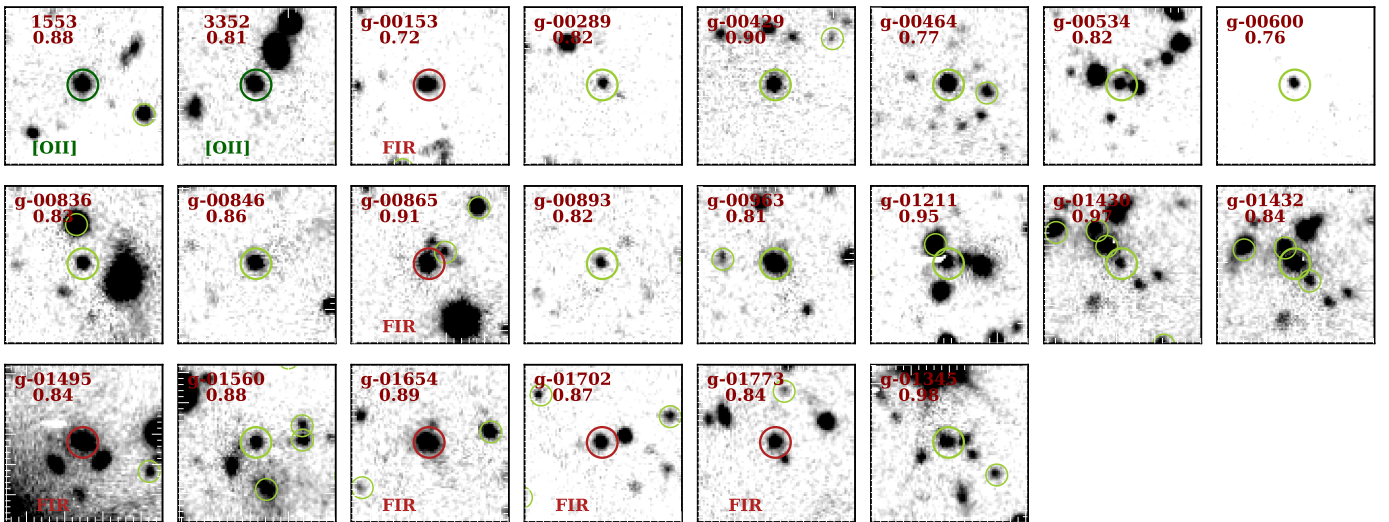


**Fig. 11.** Thumbnails of the galaxies classified as ET, according to the probability thresholds shown in Table 1 and the  $g' - z'$  colour limit imposed for the ET. Labels and circles indicate the same as in Fig. 10.

## 5. Physical properties of different morphological types

In this section, we investigate the properties of the three categories of galaxies we have identified and consider possible explanations for the unexpected population of blue ET galaxies.

First, we analysed the appearance of every morphologically classified galaxy in the  $r'$ -band, which is the image used for the classification. In Figs. 10–12, we show the thumbnails of the sources included in the three samples. As expected, LT galaxies seem more diffuse, faint, and elongated when compared to the rest. Two of them ( $g-00146$  and  $g-01209$ ) have blend problems owing to a nearby bright source, although both have  $p_{\text{ET}} \leq 0.2$ . Another two sources (4156 and  $g-00885$ ) that show a very close companion might be mergers, since in the two cases, both galaxies belong to the cluster. ET galaxies are, in general, more rounded and with the light uniformly distributed. Most of them, 17 of 24, appeared as isolated galaxies but, in contrast,

at least five of them ( $g-00865$ ,  $g-01211$ ,  $g-01430$ ,  $g-01432$ , and  $g-01560$ ) are found in apparently dense environments with many nearby galaxy cluster members. The remaining two ETs ( $g-00534$  and  $g-01495$ ) appear very close to other sources not classified as cluster members. In the third sample of blue ET galaxies, there are a variety of galaxies: clearly faint and diffuse (e.g. 1677), bright and very rounded (e.g.  $g-00505$ ), slightly elongated (e.g. 708), blended or merger (e.g. 1160), isolated (e.g.  $g-01664$ ), or inside a dense environment (e.g. 2181). Nevertheless, compared with the ET and LT samples, most of the blue ET galaxies are visually more similar to the ET ones.

Figure 13 shows the distribution of three concentration indexes ( $C_{\text{BC}}$ ,  $C$ , and GINI) for LT, ET, and blue ET galaxies. These parameters are the most stable against the effects of survey depth, spatial resolution and noise, and therefore the most reliable indicators of the morphology, especially when using the ground-based data Pović et al. (2015). In general, blue

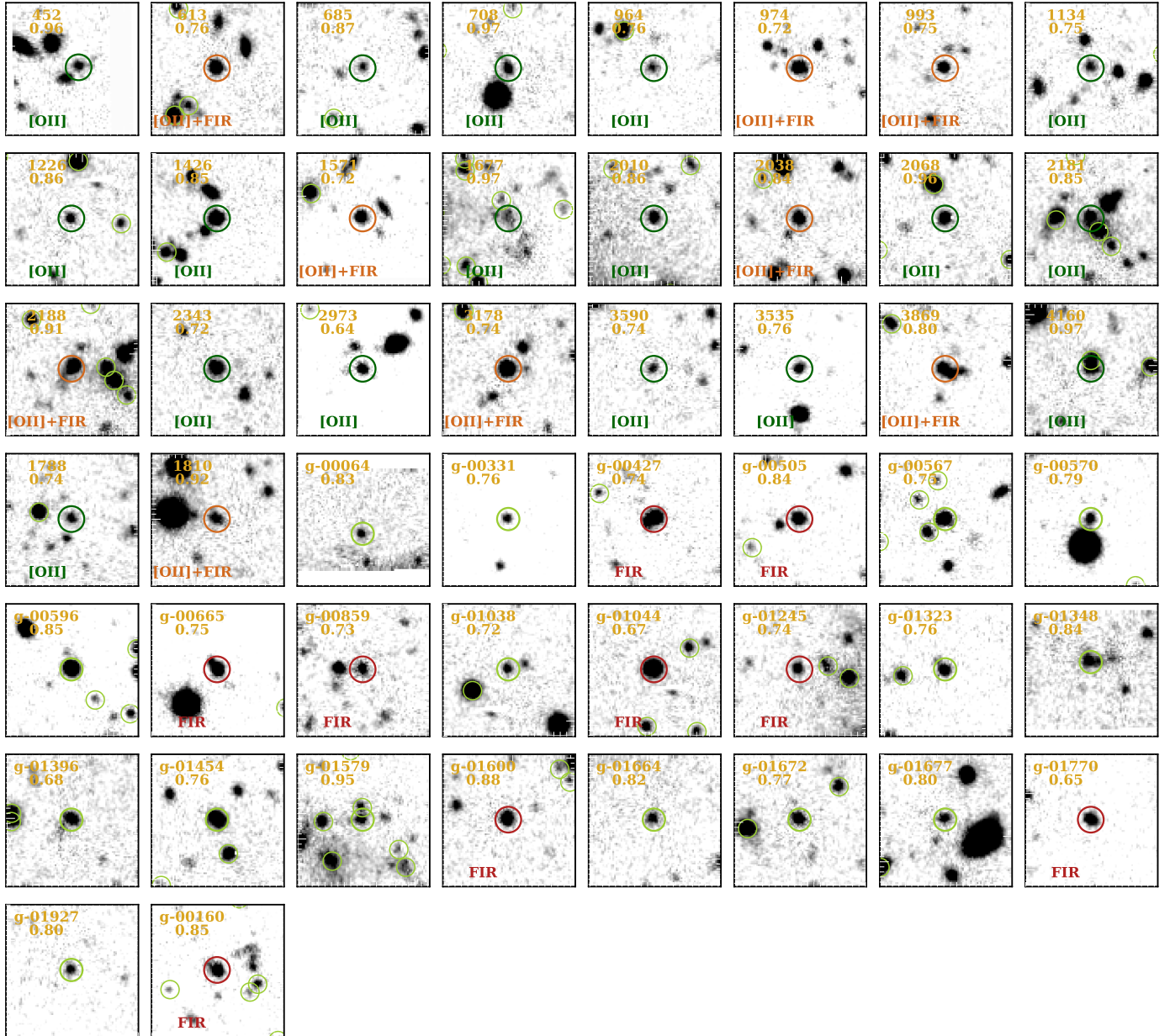


**Fig. 12.** Thumbnails of the galaxies classified as ET according to the probability thresholds (see Table 1), but that are bluer than the  $g' - z'$  colour limit considered for the ET. Labels and circles indicate the same as in Fig. 10.

ET galaxies are as concentrated as the standard, red ETs, both types being more concentrated than the LT sample. This is especially clear in the case of  $C_{BC}$  and  $C$  parameters while, in the case of GINI, the differences are less significant.

Regarding their physical characteristics, we observe in Fig. 14 the distributions of several physical parameters for each of the three morphological subsamples. In this figure, going from left to right and from top to bottom, we show the age, stellar mass, and extinction (derived through SED-fitting, as explained in Sect. 4.2 of Paper I); the size (roughly estimated as the area covered by the ellipse used by SExtractor to extract the source); the local density  $\Sigma_5$  and the cluster-centric radius as measurements of the cluster environment; and, the SFR and sSFR (calculated through Kennicutt 1998 calibrations, using the total FIR luminosity when FIR data is available and the [OII] luminosity for the remaining emitters), to gauge the star formation activity. As shown by the top vertical lines in every

panel, indicating the average value of each subsample, only the stellar mass and the sSFR seem to show a different behaviour: ET galaxies are more massive and less efficient at forming stars than the LT and blue ET samples. A Kolmogorov-Smirnov test confirmed this difference, since the statistics give a probability of almost zero than the LT/blue ET, and the ET distributions are drawn from the same parent population. Nevertheless, for the three morphological types, the average value of these physical parameters is included within the ranges defined by the average value plus/minus its standard deviation of the other morphological types, suggesting that the difference is not so significant. Considering the peak of the distributions, it seems that the blue ET population is shifted towards younger ages, however none statistical analysis confirms this fact. In relation to the environment, we find a difference in the cluster-centric distance distribution, where most of the LT galaxies are placed at distances higher than 1.5 Mpc.

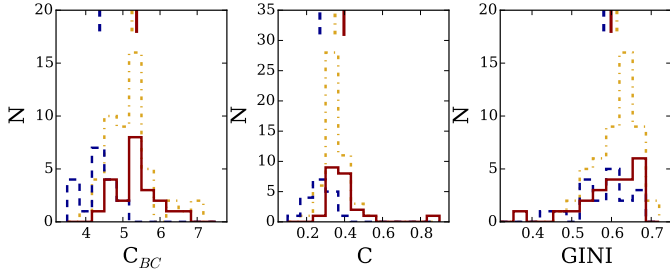


**Fig. 13.** Distributions of the morphological concentration parameters ( $C$ ,  $C_{BC}$ ,  $GINI$ ) for the three morphological samples. The LT sample is represented by the dark blue dashed line, the ET sample by the red solid line, and the blue ET sample by the yellow dash-dotted line. Top vertical lines indicate the mean values of each distribution.

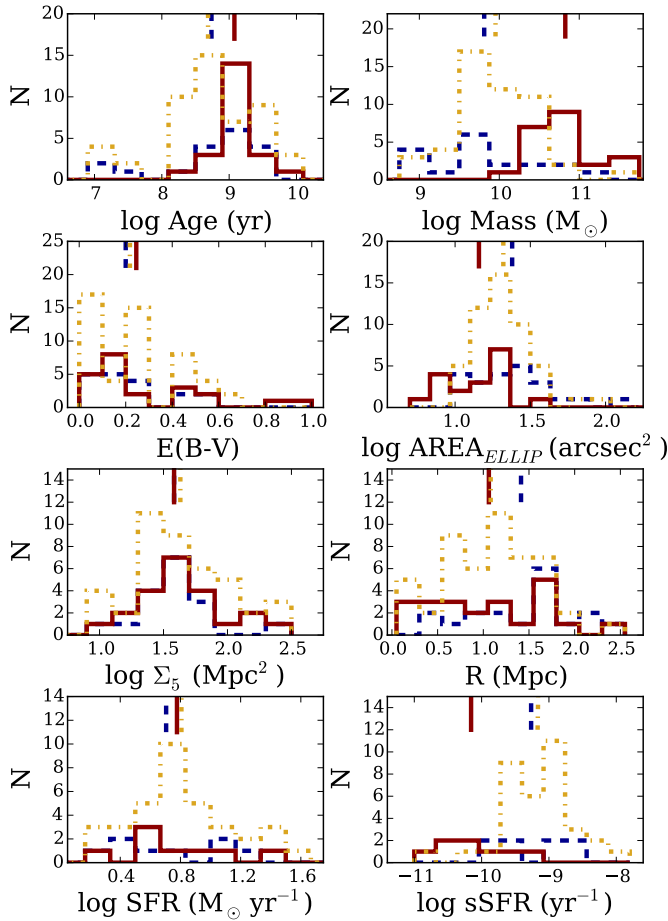


**Fig. 14.** Distributions of the physical properties for the three morphological samples: age, stellar mass,  $E(B - V)$ , size, local density, cluster-centric radius, SFR, and sSFR. The LT sample is represented by the dark blue dashed line, the ET sample by the red solid line, and the blue ET sample by the yellow dot-dashed line. Top vertical lines indicate the mean values of each distribution.

Figure 15 shows the cluster galaxy density map with the projected spatial distribution of the three morphological samples. Looking at this spatial distribution, we do not find any definitive trend. As observed through the cluster-centric distance distributions in Fig. 14, more than 70% of the LT sample is outside the virial radius, while about half of the ET populations are inside this radius. For the galaxy density we found that the three categories of galaxies show no preferred location, since

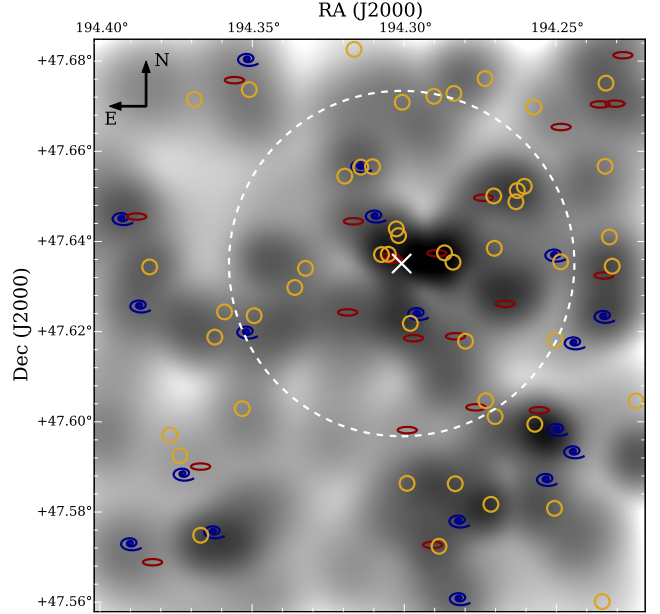


**Fig. 15.** Projected spatial distribution for the three morphological samples represented over the cluster density map. The white cross and dashed white circle are the cluster centre and virial radius, respectively. Symbols are the same as in Fig. 9.

**Table 3.** Number of LT, ET, and blue ET galaxies with emission (FIR and/or [O II]-detected), indicating the percentage relative to each morphological type.

	ET	LT	Blue ET
[O II]	2 (9%)	7 (39%)	26 (52%)
FIR	6 (27%)	3 (17%)	18 (36%)
Emitters	8 (36%)	8 (44%)	33 (70%)

they appear both in dense groups and as isolated galaxies. Qualitatively, LT galaxies are the only population avoiding the cluster core region and LT neighbours. On the contrary, the blue ET population do appear in high densities and groups that include any morphological type. In this case, there is also no relevant difference in the spatial distribution of the blue ET galaxies with respect to the ET sample. We have checked that no evidence appears if we estimate the local density with only the closest neighbour, or if we include up to the tenth neighbouring galaxies.

Finally, looking for the number of galaxies of each morphological type that show [O II] or FIR emission, the percentage of blue ET galaxies with active star formation is significantly high: while star-forming galaxies in the ET and LT subsamples are less than a half of their population, the blue ET galaxies with ongoing star formation represent 70%. In Table 3, we show the numbers and percentages of the [O II]-detected and FIR-detected galaxies, and of the emitters sample, for the three morphological types. The fact that 70% of the blue ET sample are star-forming galaxies supports the finding that the  $g' - z'$  colour is so blue. In the following section we further investigate the origin of this population.

## 6. The blue ET population

We have observed that, in general, ET, LT, and blue ET samples within the cluster show similar average physical properties. Therefore, the existence of such a blue ET population could

question its classification. In this section we analyse possible explanations for having observed these types of population, including the possibility that:

- morphological classification could be incorrect;
- redshift estimation could be incorrect;
- galaxies could be related with peculiar features;
- galaxies could host an AGN;
- the blue colours could come from photoionising post-AGB stars;
- they could be ET galaxies with current/recent star formation, and finally;
- they could be luminous compact blue galaxies (LCBG) or late-type galaxies with enhanced, centrally concentrated star formation.

In the following subsections, we discuss each of these possibilities and the analysis that we have performed.

### 6.1. Unreliable morphological classification

First, it is possible to question the performed morphological classification; however we have been very restrictive in its definition. Although some of the blue ETs might still be misclassified LT galaxies, most should be earlier types since they have very high probabilities. More than 45% of them have probabilities of being ET above 0.8, and only three sources show probabilities below 0.7.

To test the reliability of our morphological classification, and to prove that most of the blue ETs are not LT galaxies that have been incorrectly classified, we have applied the same statistical methodology to a cluster at similar redshift and using comparable imaging data that has a trustworthy morphological classification. Finding this type of cluster is not a trivial task. The selected cluster was MS1054-03 at  $z = 0.83$ . For this cluster [van Dokkum et al. \(2000\)](#) performed a visual morphological classification based on WFPC2/HST images in the *F606W* and *F814W* bands, and [Tran et al. \(2005\)](#) carried out a spectroscopic campaign with LRIS/Keck confirming 121 cluster members within the WFPC2/HST mosaic. Later this cluster was observed with the ACS/HST using *F606W*, *F775W*, and *F850LP* bands, and [Postman et al. \(2005\)](#) performed a new visual morphological classification based on these images. There is a publicly available catalogue from [Blakeslee et al. \(2006\)](#) that includes the morphological type and spectroscopic redshift of 142 members of this cluster. Regarding the available imaging data we explored two options: (i) the *F606W* WFPC2/HST available science mosaic ([Förster Schreiber et al. 2006](#)); and (ii) the Rc SuprimeCam/Subaru raw images available on request from the SMOKA Science Archive. For the first option, it is necessary to first add background noise<sup>4</sup> and then degrade to our  $r'$ -band image resolution<sup>5</sup>. For the second dataset we followed a standard data reduction process using the SDFRED1 software ([Yagi et al. 2002](#); [Ouchi et al. 2004](#)). To obtain comparable data, we used only two individual exposures, which gave us a completeness magnitude at 50% of  $R_c = 24.5$  mag. For SuprimeCam, the pixel scale is  $0.2''/\text{px}$ , and the measured seeing was compatible with our value of  $0.9''$ .

<sup>4</sup> We used the IRAF task `mknoise`, including the HST gain value, and activating the `poisson` option for the noise.

<sup>5</sup> We use the task `tgauss` within the IRAF dedicated package TFRED to equate the WFPC2 image to our pixel scale of  $0.254''$  and our seeing  $\sim 0.9$ .

Finally, we used these *F606W* and Rc processed images to execute the galSVM code, following the same methodology employed for the RXJ 1257 galaxies (as detailed in Sect. 3.3). The statistical morphological classification was performed only for those galaxies with spectroscopic redshift (thus ensuring their cluster membership) with existing visual morphological classification from [Postman et al. \(2005\)](#); furthermore we restricted the selection up to 25 mag in all bands. These conditions resulted in a sample of 137 cluster galaxies, morphologically classified with a visual methodology and detected in both HST and Subaru images. In Table 4, we show the results obtained for each image and magnitude bin, indicating for each type the number of galaxies for which the statistical and visual classification match (Good), the number of galaxies for which the statistical method fails by classifying the galaxy in another morphological type (Wrong), or by not being able to classify it (Uncl.). From the visual morphological classification, we included as LT those galaxies classified between 1 and 10, and as ET those galaxies with types between 0 and  $-5$ . We note that in this table we have omitted the fainter bin ( $24.5 < m \leq 25$ ), so the total number of objects shown for both HST and Subaru results is less than the full sample of 137 cluster galaxies. The numbers shown correspond to a standard probability threshold of  $p_{\text{ET}} - \varepsilon(p_{\text{ET}}) \geq 0.6$  to be classified as ET and  $p_{\text{ET}} + \varepsilon(p_{\text{ET}}) \leq 0.4$  to be classified as LT. From this table, it is evident that the results derived from the HST degraded image are better than those obtained with the Subaru image. This is not surprising since, although its completeness magnitude and resolution are comparable with our  $r'$  image, the S/N is worse being around two times higher for the RXJ 1257  $r'$  image. The main result that we want to test at this point is the possible fraction of wrongly classified LT galaxies: are most of the blue ET galaxies misclassified LTs and are we able to recover LTs? From the numbers in Table 4, we find that the percentage of LT galaxies misclassified as ET goes from 8(3)% for the better quality HST image to 15(6)% for the poorer quality Subaru image when estimating it with respect to the number of LT galaxies morphologically classified (when estimating it with respect to the total number of LT galaxies). From these numbers, we can confirm that the existence of this blue ET population is not caused by an incorrect classification of a large part of the LT population.

### 6.2. Unreliable cluster membership

Furthermore it is possible to cast doubts on the derived cluster membership, i.e. that these sources are at different redshifts. Nevertheless, the estimation of each source redshift to build the cluster members' catalogue has been done carefully: we have spectroscopic redshifts for 21 sources (Paper I), we obtain pseudo-spectroscopic redshifts for 87 [O II]-emitters (118 without  $v_{\text{LOS}}$  constraints, Paper III), and we estimated photometric redshifts within the cluster for 271 galaxies (Paper I) from which 64 were confirmed by the [O II]-emission line. In addition, as Table 5 shows, more than half of the blue ET population are classified with the [O II]-emission line and similar percentages ( $\sim 70\%$ ) of the photometric redshift sources are found in the three morphological types. We have compared the physical properties of the blue ET galaxies that were classified as a cluster member with their pseudo-spectra with those that were classified through photometric redshifts, i.e. blue ET galaxies [O II]-detected and -undetected. The distributions of both samples are compatible, which supports the soundness of the cluster membership classification.

**Table 4.** Classification results for the MS1054-03 cluster obtained for both HST and Subaru images, per magnitude bin.

WFPC2/HST <i>F606W</i> image			
Morpho	Good	Wrong	Uncl.
<i>F606W</i> ≤ 23			
LT = 5	4	0	1
ET = 9	2	1	6
23 < <i>F606W</i> ≤ 23.5			
LT = 10	2	0	8
ET = 16	1	0	15
23.5 < <i>F606W</i> ≤ 24			
LT = 9	3	1	5
ET = 27	10	0	17
24 < <i>F606W</i> ≤ 24.5			
LT = 8	3	0	5
ET = 23	0	7	16
SuprimeCam/Subaru <i>Rc</i> image			
Morpho	Good	Wrong	Uncl.
<i>Rc</i> ≤ 23			
LT = 12	4	1	7
ET = 29	7	10	12
23 < <i>Rc</i> ≤ 23.5			
LT = 9	6	0	3
ET = 23	4	9	10
23.5 < <i>Rc</i> ≤ 24			
LT = 7	1	1	5
ET = 20	6	2	12
24 < <i>Rc</i> ≤ 24.5			
LT = 5	0	0	5
ET = 19	4	3	12

### 6.3. Galaxies with peculiar features

Some of previous works suggested that many galaxies falling into clusters may evolve directly from peculiar, merging, and compact systems into ET galaxies without passing through the phase of regular spirals. Nantais et al. (2013) observed this by studying the morphology with HST data of a cluster at redshift  $z = 0.84$ , which is similar to ours. In this case, taking into account the poor resolution of our data, we could be missing the signs of peculiar structures, therefore detecting galaxies as earlier types, but their colours will be bluer in comparison to the standard elliptical and lenticular sources. To test this and how well we are able to detect the peculiar structures with our data, we analysed the distribution of used morphological parameters on a sample of peculiar sources that were simulated to our conditions. We selected a sample of 300 local galaxies from Nair & Abraham (2010) catalogue, classified by authors as galaxies with unusual forms and with T-Type = -99. We simulated these galaxies to map the conditions of our data, as explained in Sect. 3, and we measured the same morphological parameters. We repeated this process in five magnitude cuts that correspond to those analysed in Sect. 3.3. Finally, we compared the distributions of obtained parameters with the same ones measured for our data, to check if they map the same space of values. We run the Kolmogorov-Smirnov test, obtaining in all cases that the two distributions are significantly different. Therefore, although some of the blue ET galaxies might enter in the category

**Table 5.** LT, ET, and blue ET galaxies that were classified as cluster member by their spectrum (GMOS), by SED-fitting (photometric bands), and/or by its pseudo-spectrum (TF/OSIRIS).

Method	ET	LT	Blue ET
Spectrum	6 (23%)	2 (11%)	2 (4%)
Pseudo-spectrum	2 (9%)	7 (39%)	26 (52%)
Photometry	15 (68%)	13 (72%)	38 (76%)

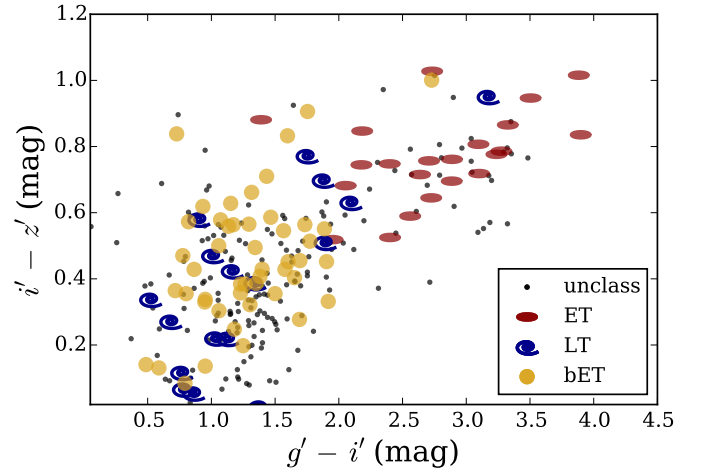


**Fig. 16.** Colour-colour diagram of RXJ 1257. Symbols are the same as in Fig. 9: blue spirals represent galaxies classified as LT, red ellipses as ET, yellow circles are blue ET galaxies, and small black dots are morphologically unclassified cluster members.

of peculiar or merging systems transforming to ETs directly, we discard the possibility that this is the case for a majority of them.

Taking into account the previous three points and the high number of galaxies classified as blue ET, we may consider that the bulk of them form a different population. As mentioned above, this population could host an AGN, could consist of ET galaxies with recent star formation activity, and/or could be related to the LCBG (Crawford et al. 2014) population.

Figure 16 shows the  $g' - i'$  vs.  $i' - z'$  colour-colour diagram of the RXJ 1257 cluster members. Following Smail et al. (1998), three types of galaxies could be analysed in this kind of diagram: 1) those with red colours, typical of passive elliptical galaxies; 2) those with blue colours typical of star-forming galaxies; and 3) those with red  $i' - z'$  colour, indicating a strong 4000 Å break and presence of older stellar populations, but with bluer  $g' - i'$  colour than in the case of group 1. The population of ~40% of the blue ET galaxies falls above the threshold  $i' - z' = 0.5$  mag, where we find the galaxies classified as standard ETs (with red colours), indicating that a large fraction of the sample shows the presence of evolved stellar populations, but with bluer  $g' - i'$  colour than red ETs. This opens the possibility that these galaxies are, or have recently been, forming stars. In the so-called transition region between 0.5 and 0.3 mag in the  $i' - z'$  colour, we found ~40% other blue ETs, while only < 20% of blue ETs are located in the bluest region.

### 6.4. AGN galaxy hosts

One possibility that cannot be ruled out is that at least a fraction of the blue ET galaxies host an AGN; the nuclear contribution could make the integrated colours bluer and eventually

place the host galaxies in the blue area of the CMD. According to the estimations of [Lemaux et al. \(2010\)](#), derived from [O II] and H $\alpha$  measurements of two clusters at similar redshift (RXJ 1821.6+6827 at  $z \approx 0.82$  and Cl1604 at  $z \approx 0.9$ ), a substantial percentage of the ELG population,  $\sim 68\%$  can be classified as AGNs and that nearly half of the sample have [O II] to H $\alpha$  EW ratios higher than unity, the typical value observed for star-forming galaxies. At the lower redshift (ZwCl 0024.0+1652 at  $z = 0.395$ ) our team ([Sánchez-Portal et al. 2015](#)) derived, using measurements of the H $\alpha$  line width and [N II]/H $\alpha$  ratios, a more modest, but also substantial percentage of AGNs, around 37%. At this stage of the survey of RXJ 1257, we only have measurements of the [O II] line and, therefore, we cannot derive the AGN fraction from diagnostics based on emission lines (e.g. [Rola et al. 1997](#)). We have four-channel IRAC photometry for 11 blue ET galaxies and therefore we can apply the MIR AGN selection criterion proposed by [Stern et al. \(2005\)](#) based on the IRAC colours 3.6–4.5 and 5.8–8.0, to get a rough idea of the importance of the AGN contamination. Of course, given the skinny sample, the results should be taken with caution. According to the authors, overall the criterion provides a robust separation of AGNs from SF galaxies, with 80% completeness and less than 20% contamination. Applied to our sample, a single galaxy (that also happens to be an [O II] emitter) out of 11 falls within the AGN region of the colour–colour space. Therefore, a crude low-limit of 10% of the population of blue ET galaxies could be guessed as hosting an AGN.

### 6.5. Photoionisation by post-AGB stars

One possibility that cannot be ruled out is that post-asymptotic giant branch (post-AGB) stars, with  $T_{\text{eff}} \sim 10^5$  K, might be at least partially responsible for the blue colours. According to [Binette et al. \(1994\)](#), the photoionisation by post-AGB stars can account for the extended ionized gas often observed in elliptical galaxies. [Ho \(2008\)](#) estimated that the nebular line emission in roughly one-third of the sources in their sample of nearby active galaxies can be powered by photoionisation from post-AGB stars. The percentage of LINERs and transition objects that could be powered by this mechanism is outstanding, 39% and 33% respectively (see also [Cid Fernandes et al. 2011](#)).

### 6.6. SF or LCB galaxies

To analyse the last two options, we split the blue ET sample into what we are going to consider ETGs with recent SF and LCBGs, but bearing in mind that this separation is purely speculative. We used the known sSFR–stellar mass correlation and the relation derived by [Elbaz et al. \(2011\)](#) for the main sequence galaxies to perform the sample division: we classified as LCBGs those galaxies placed in the starburst region, as shown in the upper panel of Fig. 17 by the shaded area; and, as ETGs with recent SF those galaxies that show normal star formation activity, being around and below the main-sequence relation, plotted with a dashed line in the upper panel of Fig. 17. This division would be equivalent if we used the SFR–stellar mass correlation from [Elbaz et al. \(2007\)](#), as shown by the solid line in lower panel of Fig. 17. Since not every blue ET galaxy has detectable star formation activity, a third sample with the rest of the so-called quiescent blue ET galaxies is defined.

[Crawford et al. \(2014\)](#) analysed the spatial and kinematic distributions of the galaxy population of a sample of five clusters at intermediate redshift  $0.5 < z < 0.9$ . The authors defined

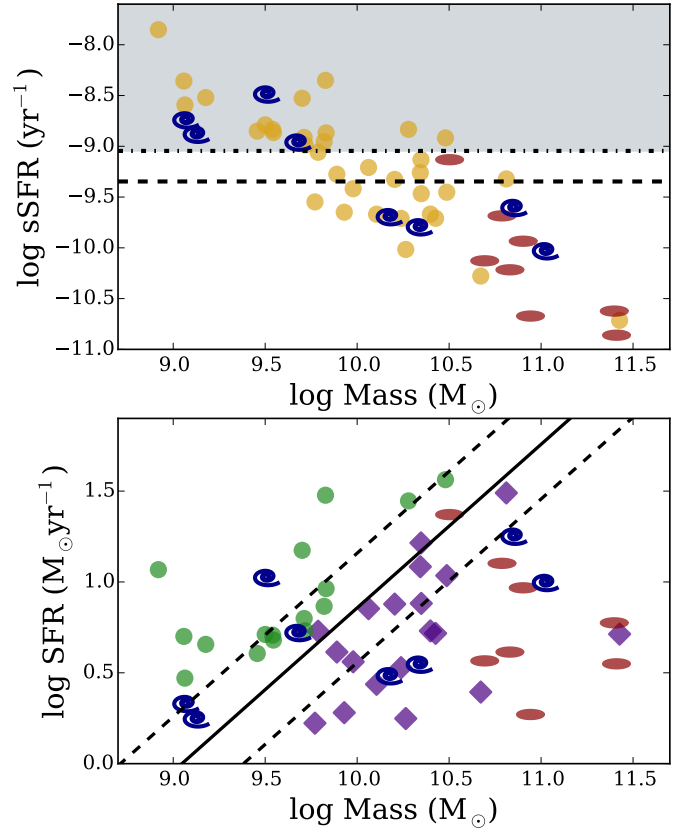


**Fig. 17.** sSFR (*top*) and SFR (*bottom*), estimated both with the FIR and [O II] emission, as a function of the stellar mass. As in previous figures, dark blue spirals are LT and red elongated ellipses are ET galaxies. In the top panel, yellow circles are blue ETs (those galaxies that by their probability are classified as ET but their  $g' - z'$  colour is below the 2 mag limit). The horizontal dashed line corresponds to the relation of [Elbaz et al. \(2011\)](#) for the main-sequence galaxies at the redshift of the cluster, and the dash-dotted line indicates the lower limit for the starburst region (grey shaded area). This line is the threshold used to split the sample into LCBGs (in the starburst area) and ETs with recent star formation (in the main sequence). In the bottom panel, green circles are LCBGs and violet diamonds ET galaxies with star formation, as classified in the top panel. The solid line indicates the  $SFR-M_*$  correlation from [Elbaz et al. \(2007\)](#), and the dashed lines show the 68% dispersion.

four galaxy samples, based only on their colour, luminosity, and surface brightness: red sequence, blue cloud, green valley, and LCBGs. The evidence they found to support the fact that the LCBG population defined was a different population is that LCBGs show a higher velocity dispersion, avoid the cluster core, and are more likely to occur in pairs or small groups, having a similar velocity to their near neighbours. To compare our blue ET population with these LCBGs, we first analysed, in Fig. 18, the kinematics for our four morphological samples, i.e. LTs, ETs, blue ETs with recent SF, and LCBGs. Figure 18 shows the radial velocity as a function of the cluster-centric radius, with the horizontal dashed lines indicating the velocity field fully covered in the OSIRIS field of view (Paper III). Visually, there is no difference between the samples. However, we obtained that the average velocity value for the LCBG sample is significantly higher than the average values for the rest ( $\sim -2500$  km s $^{-1}$  for LCBGs versus  $\sim -1100$ ,  $-880$ , and  $-560$  km s $^{-1}$  for LTs, ETs, and blue ETs with recent SF, respectively). The standard deviation values are compatible for the four samples, all showing a high dispersion with values between 2600 and 4400 km s $^{-1}$ .

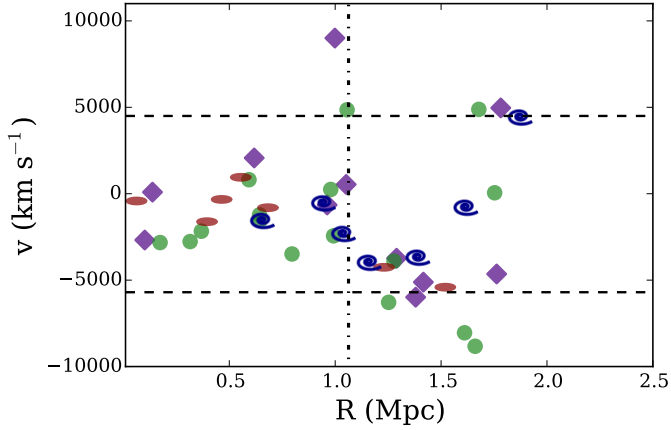


**Fig. 18.** Radius vs. radial velocity for the morphological samples: ET (red ellipses), LT (blue spirals), ET with SF (violet diamonds), and LCBG (green circles). For the rest of the blue ET sample there is no dynamical information. The vertical dash-dotted line indicates the virial radius position, and horizontal dashed lines mark off the radial velocity range full covered within the OSIRIS field of view.

Analyzing Fig. 19, we investigate the environment of each population. Figure 19 shows the probability density function (i.e. the original distribution smoothed with a Gaussian kernel density estimator) of the number of nearest neighbours, distance to the cluster core, and local density for the five morphological populations (LTs, ETs, blue ETs with recent SF, LCBGs, and the rest of the blue ETs, those we could consider as “quiescent”). Although no dramatic differences between these populations are observed, there are some notable facts: (i) the curves of the LCBG sample always have two peaks, which could indicate that it is formed of two different populations; (ii) regarding the number of neighbours within 0.1 Mpc of distance the ET and LT populations are the most isolated galaxies, while the LCBGs seem to be the most grouped, as we could expect from the Crawford et al. (2014) study; (iii) blue ET with recent SF prefer the cluster distance just above the virial radius; and (iv) there is no difference in local galaxy density except for the second peak of the LCBGs towards high densities and a large fraction of the quiescent blue ETs that appears at the lowest densities. Finally, there is a possibility that the true nature of blue ETs are LT galaxies, but with enhanced central star formation, appearing therefore as more compact and concentrated than normal LTs. They could be also responsible for the second peak of the LCBGs, or could be classified into the ETs with recent SF group.

Considering that the number of galaxies with unreliable morphological classification or photometric redshift measurements is negligible (as explained above), the analysis that we carried out suggests that the population of galaxies classified as blue ETs is formed by true early-types, being compact and concentrated, although we are not able to describe their detailed structure and kinematics. This sample of blue ET galaxies probably includes a mixture of several populations: post-interacting systems with a presence of peculiar structures, AGN hosts, galaxies with current or recent star formation, and/or LCBG. At this point, new data are necessary to confirm the presence of each of these populations. However, being a young cluster and still in formation, RXJ 1257+4738 opens the possibility for the existence of each of them, and presents a very good candidate for performing a more detailed morphological study in future.

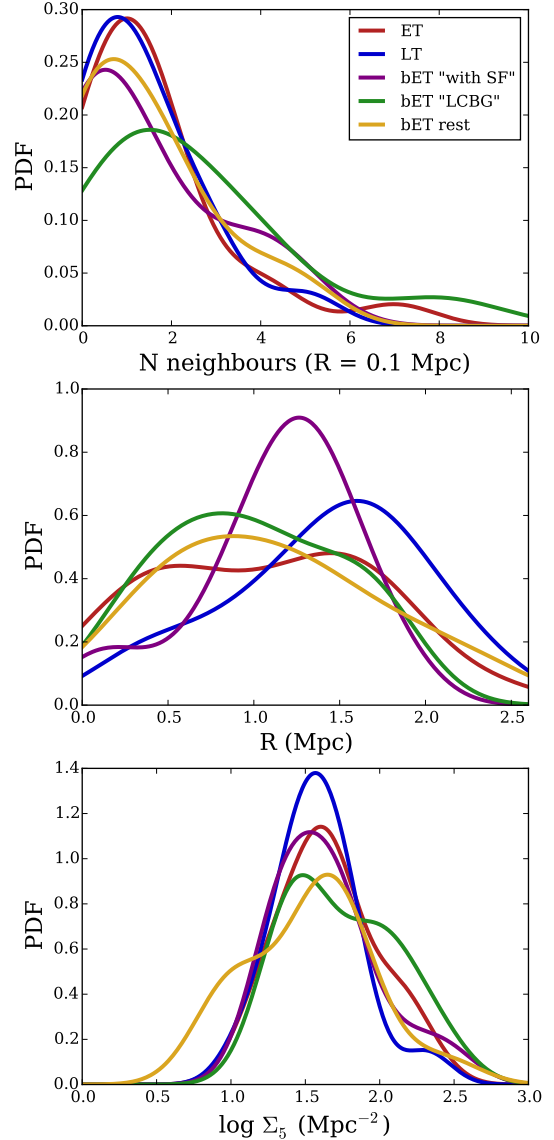


**Fig. 19.** Probability density function of the number of neighbours within a projected distance of 0.1 Mpc (*top*), the distance to the cluster core (*centre*), and the local galaxy density (*bottom*) for all the morphological types: ET (red), LT (dark blue), blue ET with recent SF (violet), blue ET LCBGs (green), and the rest of blue ETs (yellow). These curves are estimated by applying a Gaussian kernel density estimator to smooth the distribution.

## 7. Morphology-density relation

In this section, we focus our attention in the relation between the morphology of the classified cluster galaxies and their environment. Although the sample is incomplete, we have seen in Fig. 8 that there is no difference between the whole cluster and the morphologically classified samples in relation to the environment, i.e. the distributions of the local galaxy density and the distance to the cluster centre are comparable for the classified and unclassified populations.

As observed in Fig. 17, where the relation between the star formation activity and the stellar mass was analysed, the ET sample is mostly located below the main sequence, being only one galaxy in the  $s:SFR-M_*$  diagram in the region of star-forming galaxies. We also found that half of the galaxies of the other two types are clearly placed in the star-forming region.

Nevertheless, there is no clear relation between the morphological type and the average SFR, and the  $sSFR-M_*$  relation shows the stellar mass difference between massive ET and less massive LT and blue ET galaxies, indicating that stellar mass plays a more major role. Introducing the environment, calculated as the local galaxy density  $\Sigma_5$ , we analyze their dependency on those properties, the star formation activity, and the stellar mass for the different morphologies. We have observed that there is no tendency with environment, since the morphological types span the full local density range, and only the difference in stellar mass is seen (we do not show the plots since no trend became visible).

The direct relation between the cluster environment and each morphological type is approached now by analyzing the fraction of each morphological type as a function of the local galaxy density and the distance to the cluster centre. Environmental processes affect the morphological characteristics of galaxies, the morphology-density relation found by Dressler (1980) being a clear probe. In Fig. 20 we show the fractions of each morphological type as a function of the local density (left) and the cluster-centric radius (right), considering galSVM probabilities and optical colours (top) and only the galSVM classification (bottom). The fraction values and their errors in each region were estimated performing a bootstrap analysis by randomly varying the  $\Sigma_5$  and  $R$  limit values (see Paper I for more details). For the LT sample the trend is clear: they are scarce in high density regions and in the cluster centre, and their proportion grows as we move towards less dense environments and larger distances from the cluster centre. In every density region studied, the cluster environment is evident since the number of LT galaxies is always below the other morphological types. The fraction of LT galaxies on the total of the morphologically classified galaxies barely reaches the 20%, a result which is in contrast with, for example, Desai et al. (2007). In an intermediate redshift range of  $0.5 < z < 0.8$ , these authors found that typical fractions for the LT sample are approximately 55%. Our work is difficult to compare with these kinds of works because of the differences and sample incompleteness. Nevertheless, as seen in Fig. 9, we guess that the fraction of LT galaxies we obtained is highly biased since most of the unclassified cluster galaxies are placed in the fainter part of the blue cloud.

Regarding the ET samples, when we take them into account as a whole we find that they dominate the cluster core and the densest environments, and their proportion decreases opposite to the LT sample. However this evolutionary trend is really mild, specially considering the error bars. When we make the distinction using the optical colour between ET and blue ET galaxies, that trend is not evident (we have to bear in mind the error bars). On the one hand, the different shape of the ET and blue ET fractions as a function of the local density and the cluster-centric radius reflect that the effect of the local environment and the cluster potential could not be the same. Fasano et al. (2015) have recently found in a local cluster sample that, in fact, the morphology-density relation is only evident in the very inner region or in very regular clusters, while the morphology-radius relation remains unchanged for the whole sample, being only reduced for the really clumpy clusters. As discussed in Paper I, and as can be seen on the density map of Fig. 15, the RXJ 1257 cluster is still under the process of collapsing and, therefore, presents a clumpy structure, which would explain the lack of a strong morphology-density relation. The poor number statistics make it impossible for us to check the morphology-density relation in the innermost part of the cluster. On the other hand, for the ET sample the trend of increasing its number towards high density regions and at the cluster centre is possible within the

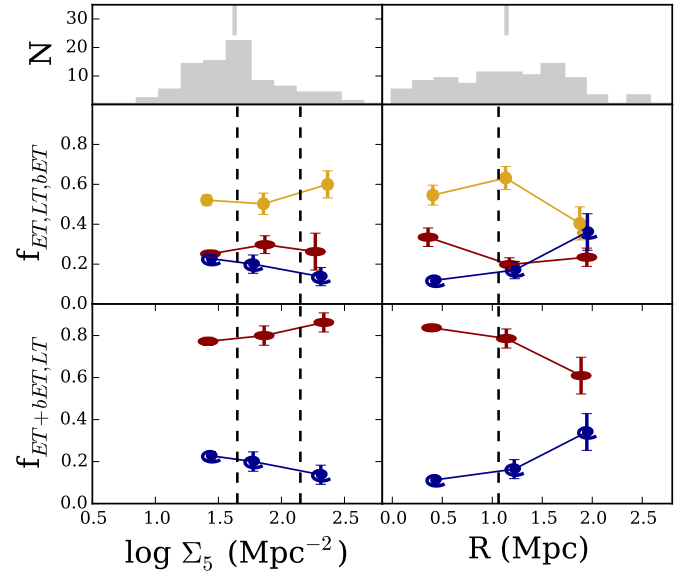


**Fig. 20.** Morphological types – LT (blue spirals), ET (red ellipses), and ET galaxies with blue  $g' - z'$  colours (yellow circles) – as a function of the local galaxy density (*left*) and the cluster-centric radius (*right*), represented as the fraction of the morphological types in three densities/radius. *Top panels:* represent the local density and cluster-centric distance distributions for the full classified sample. The vertical lines indicate the mean value of each distribution. The dashed vertical lines are the original local density limit between environments defined by KO08 (*left*) and the virial radius estimated by Ulmer et al. (2009; *right*). Error bars are estimated as the standard deviation of the fraction distribution built by bootstrap.

errors, and for the blue ET their fraction seems to grow at distances equivalent to the virial radius but also in the densest environments suggesting that this population may mainly appear as groups entering the cluster potential. Nevertheless, the fraction of blue ET galaxies is the highest in all environments at all distances, becoming the dominant population in this cluster at redshift 0.866.

## 8. Summary and conclusions

As part of a comprehensive study of the galaxy cluster RXJ 12657+4738, we have performed a morphological analysis of its cluster galaxies in the present work. Taking into account both the high redshift of the cluster and the low resolution of our optical broadband data, we decided to test the non-parametric methods to classify our galaxies morphologically. We used the galSVM code, which was tested successfully in previous works, in both cases and simulated a set of 4000 local, visually classified galaxies to the conditions of RXJ 1257 to classify the galaxies from our cluster. Our classification is statistical, providing for each galaxy the probability that it belongs to early- (E/S0) or late-type (spirals and irregulars). In the absence of better data and/or other morphological classifications, to test our classification and define the probability thresholds that ensure a reliable classification, we analysed standard morphological diagnostic diagrams and physical properties of classified sources. Being strict with the probability limits, which minimizes the possibility of a wrong classification, we classified 90 galaxies in total, ~30% of our whole sample, out of which 72 are early-types and 18 are late-types.

**Table 6.** Properties of the morphologically classified cluster galaxies (first seven rows).

ID	RA J2000 (12:mm:ss.ss)	Dec J2000 (+47:mm:ss.s)	$r'$ (mag)	Emission	A	C	GINI	S	$M_{20}$	$C_{BC}$	Probability	Morpho <sup>a</sup>
452	56:53.71	36:16.9	23.17 ± 0.05	[OII]	-3.72	0.41	0.60	-1.14	-0.98	6.65	0.96 ± 0.12	bET
613	56:55.56	38:04.6	22.60 ± 0.02	[OII]+FIR	0.05	0.35	0.68	-	-1.40	4.99	0.76 ± 0.02	bET
685	56:56.09	39:24.3	23.98 ± 0.07	[OII]	0.06	0.31	0.57	-	-1.43	5.49	0.87 ± 0.08	bET
708	56:56.02	40:30.6	23.13 ± 0.04	[OII]	0.01	0.49	0.64	0.25	-1.93	6.36	0.97 ± 0.10	bET
892	56:58.59	37:04.0	24.20 ± 0.07	[OII]	-0.01	0.26	0.67	-	-1.03	3.81	0.20 ± 0.05	LT
964	56:59.63	38:07.9	23.81 ± 0.05	[OII]	0.00	0.28	0.55	-	-1.18	4.83	0.76 ± 0.02	bET
974	57:00.09	37:06.1	22.55 ± 0.02	[OII]+FIR	0.13	0.33	0.65	-	-1.13	4.99	0.72 ± 0.03	bET

**Notes.** <sup>(a)</sup> LT: late-type, ET: early-type, and bET: blue early-type.

In the observed CMD, a large fraction of ET galaxies unexpectedly falls into the blue cloud. On another cluster with similar properties and with HST/ACS visual morphological classification available, we tested that we are able to recover LT galaxies. Therefore we can trust that ETs with bluer colours are really early-types rather than misclassified sources. We analysed the physical properties of these blue ET galaxies separately.

The main results of our analysis are:

- The comparison, among the three morphological types, of the morphological parameters, the SED-derived properties (e.g. stellar mass), and other physical properties (as those related with the environment or the star formation activity, e.g.  $\Sigma_5$  or SFR) shows no clear differences. Only the stellar mass and sSFR mean values suggest that the ET population seems to be more massive and less efficient at forming stars than the LT and blue ET samples.
- Such a blue optical colour is supported by the high percentage of blue ET galaxies forming stars, i.e. 70% of the sample.
- Neither a mistaken morphological classification nor an incorrect redshift estimation could explain the high number of galaxies classified as blue ET. These objects have ET morphologies in the sense that they are compact and concentrated, although their detailed structure and kinematics remain as open question.
- The lack of a significant difference on the properties analysed (as the spatial distribution, environment, radial velocity, or star formation activity) suggests that blue ETs might consist of a mixture of different populations. The possibilities that we analysed include: (i) galaxies with a peculiar morphology transforming directly to ETs without passing the phase of regular spirals, (ii) ETs hosting an AGN, where nuclear contribution could make the integrated colours bluer, (iii) photoionisation by post-AGB stars, (iv) ETs with recent or remaining star formation, (v) LCBGs, and (vi) LTs with star formation activity highly concentrated in their central parts. The violent environment of this cluster under the process of formation could favour the presence of these named populations.
- The analysis of the morphology-density and the morphology-radius relations becomes uncertain since not only the number statistics of morphologically classified galaxies are poor, but also most unclassified galaxies fall into the fainter part of the blue cloud (see Fig. 9), which suggest that most of them could be LT galaxies. Despite this, when only an ET/LT classification is considered, we observed a mild morphology-density and morphology-radius relation. Nevertheless, when the separation by optical colour is taken into account these relations vanish.

The significant presence of the blue early-type galaxies and lack of evident morphology-density and morphology-radius relations could be explained by the fact that RXJ 1257+4738 is not a so-called standard cluster, but a young one, being still in the process of formation and showing a clumpy structure. The work we have carried out here leaves many issues open (such as the origin of the blue ET population), but highlights the interesting case that the RXJ 1257+4738 cluster represents. There are no many similar examples in the literature to make constructive comparisons. However, we would like to emphasize once again, that all results presented in this paper in relation to morphology only reflect the situation of 30% of our cluster members. Therefore, higher resolution data are essential to obtain better and a more complete classification and to shed some light on the unanswered questions.

*Acknowledgements.* We thank I. Smail for his helpful comments. We thank the anonymous referee for her/his close reading of the manuscript and her/his valuable comments. I.P.C. acknowledges support from the Faculty of the European Space Astronomy Centre (ESAC). M.P. acknowledges financial support from JAE-Doc program of the Spanish National Research Council (CSIC), co-funded by the European Social Fund. This research has been supported by the Spanish Ministry of Economy and Competitiveness (MINECO) under grants AYA2014-58861-C3-1-P, AYA2014-58861-C3-3-P, AYA2011-29517-C03-01, AYA2010-15169 and AYA2013-42227-P, and by the Junta de Andalucía under grant TIC 114. Based on observations made with the Gran Telescopio Canarias (GTC), installed in the Spanish Observatorio del Roque de los Muchachos of the Instituto de Astrofísica de Canarias, in the island of La Palma, as part of the large ESO/GTC program ID. 186.A-2012. This research made use of Astropy, a community-developed core Python package for Astronomy (Astropy Collaboration 2013).

## References

- Abraham, R. G., van den Bergh, S., Glazebrook, K., et al. 1996, *ApJS*, **107**, 1
- Abraham, R. G., van den Bergh, S., & Nair, P. 2003, *ApJ*, **588**, 218
- Astropy Collaboration, Robitaille, T. P., Tollerud, E. J., et al. 2013, *A&A*, **558**, A33
- Bershady, M. A., Jangren, A., & Conselice, C. J. 2000, *AJ*, **119**, 2645
- Bertin, E., & Arnouts, S. 1996, *A&AS*, **117**, 393
- Binette, L., Magris, C. G., Stasińska, G., & Bruzual, A. G. 1994, *A&A*, **292**, 13
- Blakeslee, J. P., Holden, B. P., Franx, M., et al. 2006, *ApJ*, **644**, 30
- Bruzual, G., & Charlot, S. 2003, *MNRAS*, **344**, 1000
- Butcher, H., & Oemler, Jr., A. 1984, *ApJ*, **285**, 426
- Cepa, J., Aguiar, M., Bland-Hawthorn, J., et al. 2003, in *Rev. Mex. Astron. Astrofís. Conf. Ser.* 16, eds. J. M. Rodríguez Espinoza, F. Garzon Lopez, & V. Melo Martín, 13
- Chang, C.-C., & Lin, C.-J. 2011, *ACM Transactions on Intelligent Systems and Technology*, **2**, 27:1, software available at <http://www.csie.ntu.edu.tw/~cjlin/libsvm>
- Cid Fernandes, R., Stasińska, G., Mateus, A., & Vale Asari, N. 2011, *MNRAS*, **413**, 1687
- Conselice, C. J., Bershady, M. A., & Jangren, A. 2000, *ApJ*, **529**, 886
- Conselice, C. J., Bershady, M. A., Dickinson, M., & Papovich, C. 2003, *AJ*, **126**, 1183

- Crawford, S. M., Wirth, G. D., & Bershad, M. A. 2014, *ApJ*, 786, 30
- de Ruiter, H. R., Arp, H. C., & Willis, A. G. 1977, *A&AS*, 28, 211
- Deng, X.-F., He, J.-Z., Wu, P., & Ding, Y.-P. 2009, *ApJ*, 699, 948
- Desai, V., Dalcanton, J. J., Aragón-Salamanca, A., et al. 2007, *ApJ*, 660, 1151
- Dressler, A. 1980, *ApJ*, 236, 351
- Elbaz, D., Daddi, E., Le Borgne, D., et al. 2007, *A&A*, 468, 33
- Elbaz, D., Dickinson, M., Hwang, H. S., et al. 2011, *A&A*, 533, A119
- Fasano, G., & Franceschini, A. 1987, *MNRAS*, 225, 155
- Fasano, G., Poggianti, B. M., Bettoni, D., et al. 2015, *MNRAS*, 449, 392
- Förster Schreiber, N. M., Franx, M., Labbé, I., et al. 2006, *AJ*, 131, 1891
- Geach, J. E., Smail, I., Ellis, R. S., et al. 2006, *ApJ*, 649, 661
- Gunn, J. E., Carr, M., Rockosi, C., et al. 1998, *AJ*, 116, 3040
- Haines, C. P., Smith, G. P., Egami, E., et al. 2009, *ApJ*, 704, 126
- Ho, L. C. 2008, *ARA&A*, 46, 475
- Holden, B. P., Illingworth, G. D., Franx, M., et al. 2007, *ApJ*, 670, 190
- Huertas-Company, M., Rouan, D., Tasca, L., Soucail, G., & Le Fèvre, O. 2008, *A&A*, 478, 971
- Huertas-Company, M., Foex, G., Soucail, G., & Pelló, R. 2009a, *A&A*, 505, 83
- Huertas-Company, M., Tasca, L., Rouan, D., et al. 2009b, *A&A*, 497, 743
- Huertas-Company, M., Aguerri, J. A. L., Tresse, L., et al. 2010, *A&A*, 515, A3
- Huertas-Company, M., Aguerri, J. A. L., Bernardi, M., Mei, S., & Sánchez Almeida, J. 2011, *A&A*, 525, A157
- Huertas-Company, M., Kaviraj, S., Mei, S., et al. 2016, *MNRAS*, submitted [[arXiv:1406.1175](https://arxiv.org/abs/1406.1175)]
- Ilbert, O., Arnouts, S., McCracken, H. J., et al. 2006, *A&A*, 457, 841
- Kennicutt, Jr., R. C. 1998, *ARA&A*, 36, 189
- Koyama, Y., Kodama, T., Nakata, F., Shimasaku, K., & Okamura, S. 2011, *ApJ*, 734, 66
- Lemaux, B. C., Lubin, L. M., Shapley, A., et al. 2010, *ApJ*, 716, 970
- Lotz, J. M., Primack, J., & Madau, P. 2004, *AJ*, 128, 163
- Martini, P., Miller, E. D., Brodwin, M., et al. 2013, *ApJ*, 768, 1
- Nair, P. B., & Abraham, R. G. 2010, *ApJS*, 186, 427
- Nantais, J. B., Flores, H., Demarco, R., et al. 2013, *A&A*, 555, A5
- Oke, J. B., & Gunn, J. E. 1983, *ApJ*, 266, 713
- Ouchi, M., Shimasaku, K., Okamura, S., et al. 2004, *ApJ*, 611, 660
- Pintos-Castro, I., Sánchez-Portal, M., Cepa, J., et al. 2013, *A&A*, 558, A100
- Postman, M., Franx, M., Cross, N. J. G., et al. 2005, *ApJ*, 623, 721
- Pović, M., Sánchez-Portal, M., Pérez García, A. M., et al. 2012, *A&A*, 541, A118
- Pović, M., Huertas-Company, M., Aguerri, J. A. L., et al. 2013, *MNRAS*, 435, 3444
- Pović, M., Márquez, I., Masegosa, J., et al. 2015, *MNRAS*, 453, 1644
- Rola, C. S., Terlevich, E., & Terlevich, R. J. 1997, *MNRAS*, 289, 419
- Sánchez-Portal, M., Pintos-Castro, I., Pérez-Martínez, R., et al. 2015, *A&A*, 578, A30
- Schawinski, K., Lintott, C., Thomas, D., et al. 2009, *MNRAS*, 396, 818
- Smail, I., Edge, A. C., Ellis, R. S., & Blandford, R. D. 1998, *MNRAS*, 293, 124
- Stern, D., Eisenhardt, P., Gorjian, V., et al. 2005, *ApJ*, 631, 163
- Tanaka, M., Kodama, T., Arimoto, N., et al. 2005, *MNRAS*, 362, 268
- Tonnesen, S., & Cen, R. 2014, *ApJ*, 788, 133
- Tran, K.-V. H., van Dokkum, P., Franx, M., et al. 2005, *ApJ*, 627, L25
- Tran, K.-V. H., Papovich, C., Saintonge, A., et al. 2010, *ApJ*, 719, L126
- Ulmer, M. P., Adami, C., Lima Neto, G. B., et al. 2009, *A&A*, 503, 399
- van Dokkum, P. G., Franx, M., Fabricant, D., Illingworth, G. D., & Kelson, D. D. 2000, *ApJ*, 541, 95
- Vulcani, B., Poggianti, B. M., Fritz, J., et al. 2015, *ApJ*, 798, 52
- Webb, T. M. A., O'Donnell, D., Yee, H. K. C., et al. 2013, *AJ*, 146, 84
- Wolf, C., Aragón-Salamanca, A., Balogh, M., et al. 2009, *MNRAS*, 393, 1302
- Yagi, M., Kashikawa, N., Sekiguchi, M., et al. 2002, *AJ*, 123, 66
- Ziparo, F., Popesso, P., Finoguenov, A., et al. 2014, *MNRAS*, 437, 458
- Zwicky, I. F. 1942, *ApJ*, 95, 555